Spring 2018

UNINTENTIONAL RF RADIATION AND RECEPTION IN COAXIAL CABLE TRANSMISSION LINES DUE TO SHEATH CONDUCTOR FAULTS

Ronald Totten
University of New Hampshire, Durham

UNINTENTIONAL RF RADIATION AND RECEPTION IN COAXIAL CABLE TRANSMISSION LINES DUE TO SHEATH CONDUCTOR FAULTS

BY

RONALD J. TOTTEN

Bachelor of Science in Computer Engineering, University of New Hampshire, 2017

THESIS

Submitted to the University of New Hampshire

in Partial Fulfillment of

the Requirements for the Degree of

Master of Science

In

Electrical Engineering

May 2018

This thesis has been examined and approved in partial fulfillment of the requirements for the degree of Master of Science in Electrical Engineering by:

Thesis Director, Nicholas J. Kirsch, Ph.D.

Associate Professor

Department of Electrical and Computer Engineering

Kent Chamberlin, Ph.D.

Professor and Chair

Department of Electrical and Computer Engineering

Michael J. Carter, Ph.D., P.E.

Associate Professor

Department of Electrical and Computer Engineering

On May 2, 2018

Original approval signatures are on file with the University of New Hampshire Graduate School.

DEDICATION

I would like to dedicate this thesis to my wife, Lanta Totten, and to my children, Liz, Turner, Emerson, and Declan. Without the boundless support and sacrifice of whom this work would not have been possible.

ACKNOWLEDGMENTS

I would like to thank my advisor, Dr. Nicholas Kirsch, for his support of my academic goals, and for his mix of patience and candor in guiding my efforts. Likewise, I owe a debt to the other members of my committee, Dr. Kent Chamberlin and Dr. Michael Carter. Their continued encouragement and enthusiasm throughout my research was of immense value both technically and inspirationally.

I would also like to thank my fellow graduate student, Cyle Ziegler, whose expertise with computer modeling, among other things, was instrumental in the development of this work.

TABLE OF CONTENTS

LIST OF TABLES

LIST OF FIGURES

LIST OF ACRONYMS

HFC	Hybrid Fiber Coaxial
RF	Radio Frequency
CATV	Community Antenna Television (or Cable Television)
LTE	Long-Term Evolution
EMI	Electromagnetic Interference
OSP	Outside Plant
VNA	Vector Network Analyzer
MTTR	Mean Time to Repair
QAM	Quadrature Amplitude Modulation
OFDM	Orthogonal Frequency Division Multiplexing
CNR	Carrier-to-Noise Ratio
SCTE	Society of Cable Telecommunications Engineers
bps	Bits per Second

ABSTRACT

UNINTENTIONAL RF RADIATION AND RECEPTION IN COAXIAL CABLE TRANSMISSION LINES DUE TO SHEATH CONDUCTOR FAULTS

by

Ronald J. Totten

University of New Hampshire, May 2018

Despite the ever-growing amount of fiber optics deployed in wireline communications networks, coaxial cable is still a significant component. It is present in the radio frequency (RF) portion of hybrid-fiber-coaxial (HFC) communications networks typically employed in cable telecommunications (CATV) systems which service the majority of US households. Sheath faults in coaxial cables are a common problem for the industry and lead to unwanted and costly ingress or egress of signals into or out of the network.

Common-mode currents have been previously identified as a source of ingress or egress for a variety of shielded cables in a number of industrial applications. This paper analyzes the electromagnetic properties of coaxial cable sheath faults to demonstrate that common-mode currents are the principal mechanism explaining the observed radiative properties of such faults, particularly in the lower frequency ranges, e.g. the 5-42 MHz upstream band employed by most U.S. cable system operators. Empirical measurements from coaxial test segments of a variety of sheath faults and configurations are shown to be consistent with results from computer simulations and analytical models of the physical

samples. These results in turn are found to support conversion between common-mode and differential-mode currents as the primary causative agent.

These findings can be used to better understand the causal mechanisms and requisite conditions for ingress and egress to develop in communications networks, and thereby improve methods to detect, remediate, and prevent sources of network impairment arising from compromised coaxial sheath conductors.

CHAPTER 1 – INTRODUCTION

1.1 Motivation

In broadband wireline communications networks, such as the Hybrid Fiber Coaxial (HFC) architecture employed widely by cable telecommunications operators, physical faults in the network components that compromise radio frequency (RF) shielding are problematic for several reasons. Such networks are ideally meant to be fully contained secondary users of the bandwidth over which they operate, typically 5-1200 MHz. Legal limitations on the level of signal egress, or "leakage", escaping over the air exist and are enforced by the FCC [1]. Also, compromised RF shielding provides opportunities for ambient signals (e.g., from primary users) to be introduced as interference onto the network, "ingress" [2, 3], compromising its performance [4,5]. The existence, detection, and remediation of such ingress/egress sources pose ongoing challenges for the telecommunications industry and consume considerable time and resources.

Although hard numbers on labor hours spent and costs associated with ingress- and egress- related network faults are difficult to come by due to their proprietary nature, one study published in 1997 found that 14% of network downtime was related to return path noise. It also found that these ingress-related network outages had a mean-time-to-repair (MTTR) of about two hours [6]. These numbers do not take into account the significant amount of technician time spent proactively addressing ingress or egress

issues in order to prevent them from becoming service outages. Also, the relative importance of return path ingress-driven events has almost certainly increased since the time of that study given the marked increases in the subscriber data rates offered by cable service providers, and the increase in the number of data customers serviced by the industry, which has grown to about 65 million subscribers in the U.S. alone as of 2017 [7]. Such maintenance and corrective activities, then, can be seen to comprise a non-trivial component of an industry that generates $48B in yearly economic activity [7].

Another driver for interest in sources of return path ingress is that it can reduce the data rates that can be supported by a network. Within the available return path spectrum of approximately 5-42 MHz, prevalent ingress noise tends to make the band below about 16 MHz unusable for communications carriers [3]. In the balance of the return path band, quadrature amplitude modulation (QAM) or, more recently, orthogonal frequency division multiplexing (OFDM) signals are used to transmit information [2]. For these signals an upper limit exists on the modulation order given the carrier-to-noise ratio (CNR) environment of the transmission channel. Higher orders of modulation, for example 64QAM versus 16QAM, have higher data rates for a given bandwidth (6 bits/second/Hertz and 4 bits/second/Hertz, respectively) but require a higher CNR to operate. Specifically, it has been shown that for every 3 dB change in CNR a corresponding gain or loss of 1 bps/Hertz will be observed in the data carrying capacity of the channel, all other things being equal [2]. Therefore, the prevention, detection, and mitigation of return path ingress has a direct bearing on the data rates that can be offered to customers. It is worth noting that the CATV industry in aggregate has spent an annualized $27.5B per year for the last

two decades on infrastructure improvements aimed largely at increasing available bandwidth and data rates [7]. For the case of egress signals emanating from CATV networks, violation of FCC mandated emission thresholds can result in fines, or in extreme cases, forced network shutdowns [1]. As a result, signal leakage detection and repair programs are a regular part of CATV plant maintenance technicians' duties [8].

Compounding these problems is the fact that the electromagnetic properties of such network faults are poorly understood, and often exhibit what may be counterintuitive values for characteristics such as resonant frequency. Historically, testing to identify sources of signal leakage in HFC networks was performed exclusively in the aeronautical band (108-137 MHz) [2] under the assumption that signal leakage would be roughly comparable at a broad range of frequencies [4, 8], but recent work has identified that network faults can produce frequency selective ingress/egress points of a variety of resonant frequencies and bandwidths, including the 700-850 MHz long-term evolution (LTE) wireless communications band [8], and the 5-42 MHz band [3] used for upstream voice and data communications in HFC networks. The latter is perhaps an unobvious result given that the typical sheath faults in question have physical aperture sizes which are on the order of 1/10,000 of the wavelengths in the CATV upstream band (Fig. 1). Typical examples of such faults include poor connector contact, radial sheath cracks, or a variety of holes produced by various mechanisms in the outer coaxial conductor (Fig. 2) [8]. Some prior work classifies these as *soft faults*, which, as compared with *hard faults*, produce only very small changes in the impedance of the transmission line, are harder to detect, e.g., with reflectometry, and are not as well represented in the literature [9, 10].

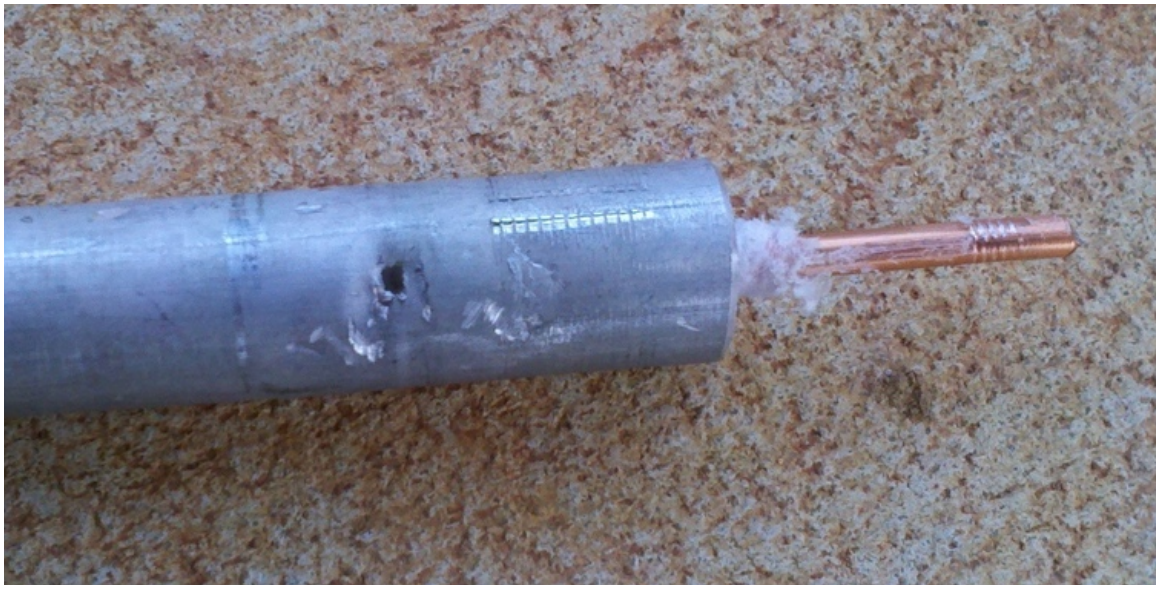

Fig. 1. Small (~2mm) hole in 0.500” coaxial cable caused by tooling

Fig. 2. Abrasion from wind motion (top) and holes from electrical arcing (bottom)

1.2 Objectives

The goal of this work is to establish a theoretical framework that explains the strong ingress/egress characteristics in the 5-50 MHz band that is exhibited by a significant subset of coaxial cable faults in HFC networks. For example, one industry study found that 59% of network faults detected were dominant in this band [11]. An underlying hypothesis of this work is that if models can be created of coaxial cables with sheath faults based upon physical exemplars known to exhibit the phenomenon of interest, and which in turn produce results consistent with real-world observations, they can be used to explore the relevant physical and electromagnetic properties giving rise to the observations.

1.3 Method

To accomplish the objectives outlined above, test segments are produced from coaxial cable such as is used in HFC networks. These include an undamaged cable and a series of segments which bear sheath conductor damage physically similar to that which would arise naturally in coaxial cables installed as part of a wireline communications network. Next, computer models of undamaged and damaged cable segments are generated using the HFSS electromagnetic field simulation package [12]. The physical and simulated observations from the undamaged segment form the baseline expectations of cable performance. The simulations of damaged cables utilize some degree of geometric idealization of the faults, such as those employed effectively by Manet *et al* [9], Cerri *et al* [13] and Lundquist *et al* [14]. A hypothesis of this work is that common-mode

currents that arise in cables as a result of sheath faults are likely a significant causal mechanism for the observed phenomena. To this end, parameters of several of the models are explored with a focus on properties that might give rise to common-mode currents, such as elevated contact resistance, parasitic inductance, and/or fault gap capacitance. Simulated results are compared with physical measurements of the test cables, including presumed radiative losses, ambient ingress reception, frequency response, and S-parameters. Factors such as overall cable length, relative fault position along a cable, and various forms of connectorization and termination are also assessed to determine their impact on the phenomena of interest.

The contribution of this work is that it identifies the principal causal mechanism responsible for the observed ingress and egress behavior of coaxial sheath faults on cables of the sort employed in CATV networks. This better understanding of the electromagnetic properties of such faults and their relevant physical parameters can provide insight into the requisite conditions for ingress or egress to arise, given some physical damage or other compromise to the sheath conductor. It can also be applied to improve methodologies to prevent, diagnose, or repair ingress or egress sources, with potential to reduce the considerable time, effort, and money expended by wireline communications operators to harden their networks.

1.4 Organization

The rest of this document is organized as follows: Chapter 2 provides background for this work. Prior efforts to assess the electromagnetic properties of coaxial and other shielded cables are discussed. Methods for modeling coaxial sheath faults are explored,

as are the mechanisms of common-mode currents that can arise in shielded cable. The radiative properties resulting from common-mode currents are also examined along with techniques to measure the magnitude of such effects

Chapter 3 details how the empirical tests were designed. This includes the methodology for fabrication of test samples, as well as descriptions of setups for the various testing regimes employed. Similarly, chapter 4 details the implementation of electromagnetic computer models designed to represent physical test cable specimens.

Chapter 5 discusses and compares the results of the tests and simulations performed. Support for the hypothesis of this work is examined, and conclusions in favor of it are reached. Lastly, future work is contemplated.

CHAPTER 2 – BACKGROUND

As mentioned above, HFC networks are intended to be closed systems that are designed to avoid electromagnetic interference (EMI) with other systems and minimize intrusion of outside signals onto their communications channels. In the case of the former, this is not merely good engineering practice, but mandated by FCC regulations which impose limitations on the maximum allowable field strength that can escape from such networks in specified frequency bands [3]. For the latter, as secondary users of the bandwidth, HFC networks must be designed to operate in an environment potentially permeated with external signals in their operational frequency range. Ideally, this entails preventing those external signals from entering the network [8]. Network signals escaping into the environment, or *signal egress*, and external signals making their way into the network, or *signal ingress*, as discussed above, are significant and costly problems for the CATV industry. The term *signal leakage*, or alternately EMI, is sometimes used to refer to both ingress and egress phenomena collectively, and that convention is used in this paper. Also, the principle of reciprocity affords that the study of signal egress for some particular case in question, i.e. radiation from the cable of some signal within it, can be seen as interchangeable with the inverse situation where the same fields present outside the cable can be seen as the source, as from some external transmission, and are responsible for generating an ingress signal within the cable. This principle is heavily utilized in this work where, in various test cases, either signal ingress or signal egress is

observed. In all such cases it is understood that one can be seen as a proxy for the other. Critically, this isometry between radiation and reception only holds for a particular frequency. Put another way, it would not be appropriate to compare the reception at one frequency with the radiation at another. This may seem to be an obvious constraint, but it was once a widely held industry belief that ingress or egress sources would be roughly equally present across the operating frequency range. However, as mentioned above, recent work has established that such sources exhibit frequency selectivity, and that measurement in one frequency range, say the aeronautical band, cannot be used to reliably make determinations about another, for example the HFC upstream or the LTE band [3, 8].

HFC networks are comprised of fiber optic segments feeding distribution areas that utilize radio-frequency signals carried on coaxial cables. Since HFC networks are generally bidirectional, an opto-electronic device bridges the two domains by converting optical signals into RF for the *downstream* signals, or the reverse conversion for *upstream* signals. The latter is sometimes also referred to as the *return path*, since it contains signals originating with the subscribers at the end-points of the network. In the United States the typical operating bandwidth for downstream signals is 50 MHz to as high as 1.2 GHz, while upstream signals for CATV systems generally operate between 5 MHz and 42 MHz, with a narrow, unused guard-band between the two. The RF portion of the network is comprised of coaxial cables interconnecting various pieces of equipment, such as splitters or signal-boosting amplifiers, that form a tree structure providing for connectivity to all the desired endpoints in a geographical footprint (homes, businesses,

etc.). These coaxial cables are made of a solid aluminum outer conductor, a copper-clad aluminum center conductor, and a polyethylene foam dielectric. These cables range in size but are generally between 0.5 and 0.875 inches in outer diameter. Smaller diameter, flexible coaxial cables, such as RG-6, provide connection from the network to subscriber premises. The characteristic impedance of coaxial cables used in CATV networks is 75 Ω.

The optical portions of an HFC network are inherently immune to EMI. The RF portions, while not immune, are ideally shielded from EMI. This is accomplished by using shielded, i.e. coaxial, cables and terminating the outer, shielding conductor directly to the enclosed metal housings of all network equipment and terminations. When correctly installed and undamaged, this practice produces an electrically contiguous RF shield across the entire extent of the RF portion of the HFC network. In this state it would not be expected to see electromagnetic fields originating internal to the network to extend beyond the shield, and likewise external fields should not be found to have a net influence on the internal regions of the transmission lines.

In practice, however, HFC networks have been found to be less than ideally shielded. They are commonly sources of signal egress and impaired by signal ingress to one degree or another. This has been noted in work by Nakamura *et al* [4], Haelvoet *et al* [5], Sandino *et al* [6], publications by the SCTE [8], and prior work of this author [3]. The problem of return path ingress in HFC networks is compounded by the fact that the tree structure of the network (in terms of the downstream signals) acts as a “noise-funnel” from the perspective of the upstream signals, since ingress admitted at any and all

locations within a service area are ultimately combined together at the point of RF-to-optical conversion [5].

There is broad agreement on causes of compromised shielding, which include loose or poorly installed connectors, poor contact between mating surfaces of network equipment housings, radial cracks in the outer conductor of coaxial cables, and a wide range of holes and penetrating abrasions in the outer conductor [8]. These are in turn explained variously by poor craftsmanship, wind-induced motion or other vibration, thermal cycling, lightning strikes, water infiltration, arcing from contact with power cables, and rodent damage (most especially squirrels). While these shield faults are correctly identified as the proximal causes of signal leakage for HFC networks, the causal mechanisms that allow such faults to generate ingress or egress in the frequency ranges observed has been less well explored, particularly as related to sources arising from the coaxial cable itself. Investigation of coaxial sheath faults in the literature *has focused mainly on their impact on coaxial cable transmission properties*, such as return loss and reflectometry, as opposed to the radiative (or, equivalently, receptive) properties. Despite the difference in emphasis, these studies have nonetheless made a number of important insights that this present work builds upon.

For example, Manet *et al* [9], Cerri *et al* [13], and Lundquist *et al* [14] each explored partial annular interruptions in the sheath conductor of somewhat smaller (compared with those studied in this work), flexible coaxial cables, focusing mainly on the reflection coefficient of various fault configurations. They all concluded that the principal effect of such faults is a slightly elevated inductance in the section with the fault, and that this class

of faults produces only minimally elevated return losses. All three groups also found that such faults were difficult to detect using reflectometry outside of a lab setting due to the very small level of reflected power. Because of this, Manet *et al* classify these as *soft faults*, as compared with *hard faults* that are more easily detected by virtue of their greater impedance change relative to nominal and higher reflection coefficient [9]. Cerri *et al* went on to assess complete annular interruptions in the sheath as well and found that a lumped-element model could conceptually be used to represent them, with a series resistance and series capacitance representing the fault's effects on impedance. They concluded however, that in practice a full-wave analysis was more appropriate given the inherent frequency dependence of the assumed lumped-element model components [13]. The analytical approach based on the method of moments employed to arrive at the reflection coefficient were further detailed in an earlier work by Cerri *et al* and, while radiation was still not the focus, this did take into account the presence of radiation from the shield gap itself [10]. However, in the frequency ranges of interest for this work, principally 5-50 MHz, such a radiative mechanism seems unlikely to account for the observed signal leakage given the size of the fault apertures relative to wavelengths in question, which are on the order of 10 m or longer.

In the ideal operation of shielded transmission lines, current flowing on the center conductor(s) is equal in magnitude but opposite in direction to current traveling on the interior surface of the shield, which results in essentially no net electric field external to the sheath conductor. These are known as differential-mode currents. Common-mode currents are those that travel on the center conductor(s) and the sheath in the same

direction, and therefore the fields do not cancel out. Under certain conditions differential-mode currents can be converted to common-mode currents, or vice-versa. Where such conversion occurs, it produces egress or ingress, respectively, on otherwise shielded transmission lines.

It has been shown that common-mode to differential-mode conversion is a significant mechanism for EMI in a wide range of applications involving a variety of shielded cable types. Work by Brown has demonstrated common-mode currents to exist and to be a cause of ingress on shielded multi-conductor cables commonly used in audio processing equipment [15]. In that work, the fact that the shield conductor was indirectly connected to the chassis ground via the processing equipment electrical ground was implicated as the source of common-mode currents (Fig. 3a). In work by Han [16] and Liu *et al* [17] a similar configuration involving coaxial cables was explored. In their works, a coaxial transmission line was terminated with a normal load at one end, while on the other end the sheath bypassed the chassis ground and was connected to electrical ground by a length of wire (Fig. 3b). It was shown that this configuration, which they refer to as a *pigtail termination*, was responsible for the development of common-mode currents and that these currents were responsible for signal leakage in the cable. With some inspection, it is apparent that the circuit in Fig. 3a and the circuit in Fig. 3b are electrically very similar to one another, and both have been shown in the work cited above to be sources of both common-mode currents and, as a result, signal leakage. The circuit shown in Fig. 3c represents a coaxial transmission line with a sheath fault, which is the subject of this work. It can be seen that points A, B C, and D from this figure correspond

to the same labeled points in Fig. 3b, and that the coaxial sheath fault diagram is essentially two instances of Fig. 3b back-to-back. It is therefore expected that coaxial sheath faults might exhibit properties similar to the prior two circuits, and to lend themselves to similar analysis. In particular, analytical models and full-wave simulations developed by Liu *et al* demonstrated that common-mode currents can arise as a result of sheath-based impedance mismatches in the coaxial line, which, in their work, was due to the pigtail termination. Furthermore, they showed that a coaxial cable segment with common-mode currents can be modeled as an equivalent dipole antenna with parameters derived from physical parameters of the cable and the mismatch [17].

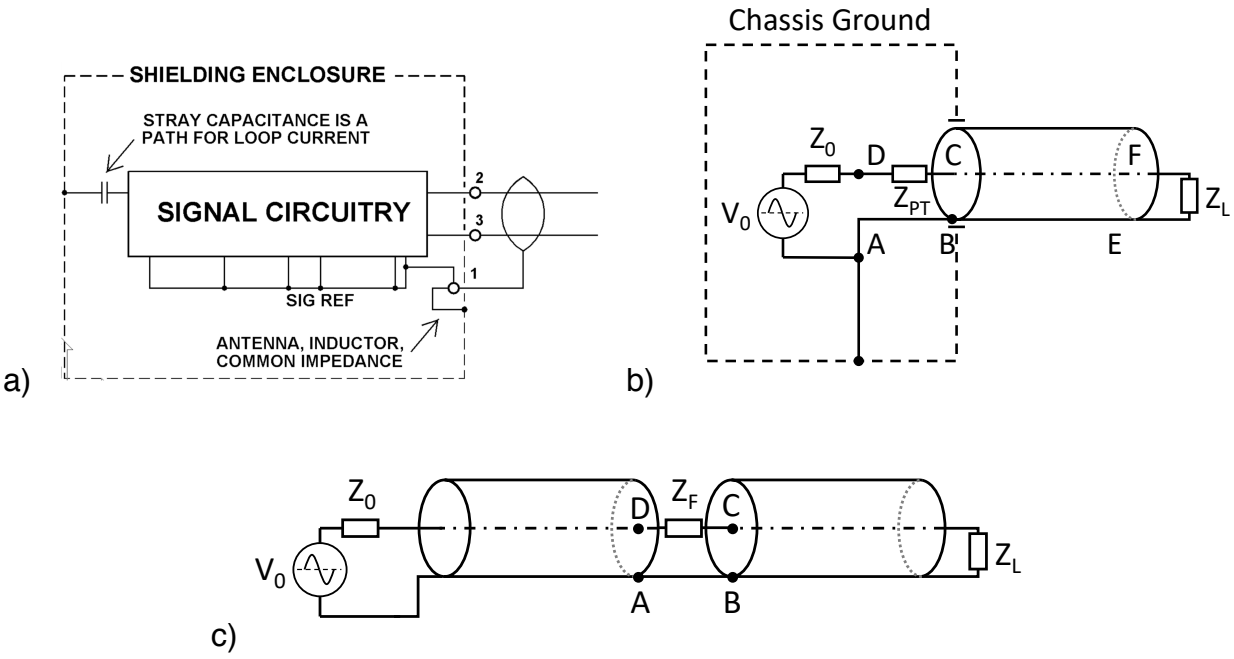

Fig. 3. Examples of circuits exhibiting common-mode current

a) Circuit exhibiting common-mode reproduced from Brown [15]; b) “Pigtail” coaxial termination adapted from Han [16]; c) Coaxial sheath fault of the type studied in this work

Hayashi *et al* explored the related problem of poor connector contact and its role in the production of common-mode currents [18-21]. Interestingly, the

simulations and physical experiments of several of these studies modeled a connector with poor contact by removing an annular section of a flexible coaxial cable's shield, and then bridging that gap by various combinations of film resistors [18, 19]. A depiction of the model from Hayashi *et al* is reproduced in Fig. 4a, and it is strikingly similar to models developed for this work, for example the bridged-gap radial crack-fault model shown in Fig. 4b. It was found by Hayashi *et al* that the strength of common-mode currents, and by extension ingress or egress magnitude, was proportional to the resistance of the bridging contact points. Conversely, as the bridging resistance approached 0 Ω (at DC), common-mode currents became minimal [19].

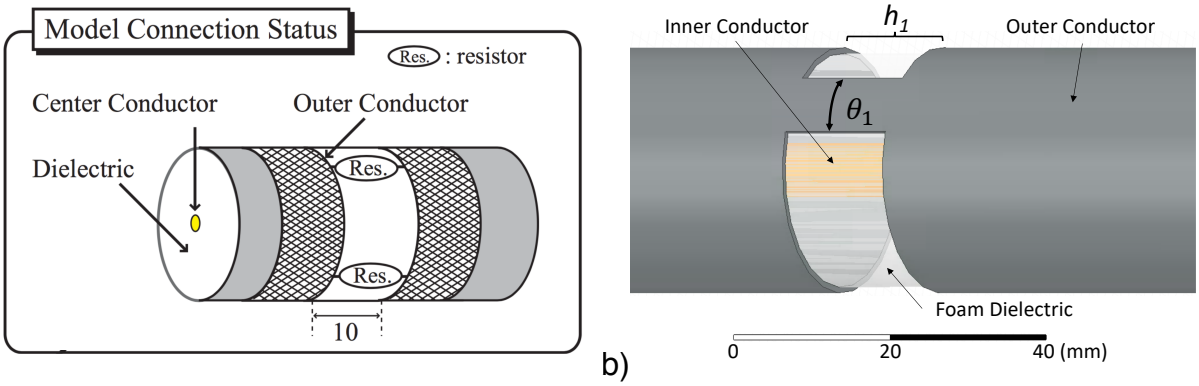

Fig. 4. Comparison of fault models

Consistent results were obtained in later work by Hayashi *et al* [20] where an actual loose connector was used in place of the experimentally-more-stable proxy used by them in earlier studies [18, 19]. Using reflectometry, it was determined that the magnitude of common-mode currents was proportional to parasitic inductances which can form on loose connectors in addition to resistive contact points. This inductive factor has a frequency dependence arising from its inductive reactance, ωL [20]. Using a model similar to the one shown in Fig. 4a, still later work by this group determined through simulation

that inductive effects tend to be overwhelmed by resistive effects as gap resistance increases [21].

Additionally, prior work has supported the premise that numerical or computer simulations can be generated which reproduce real-world measurements of coaxial sheath faults with good fidelity [9, 10, 13, 14]. Likewise, it has been demonstrated that related conditions, such as faulty or suboptimal cable connectorization or terminations giving rise to signal ingress/egress can be successfully simulated [18-21, 22]. In the present work, 3-D electromagnetic models of various sheath fault conditions have been generated using the HFSS electromagnetic field simulation package. Results from these simulations are compared with empirical observations of the physical exemplars the models are based on, as well as with results from prior work. Details of the simulations and the parameters derived from them are given in chapter 5.

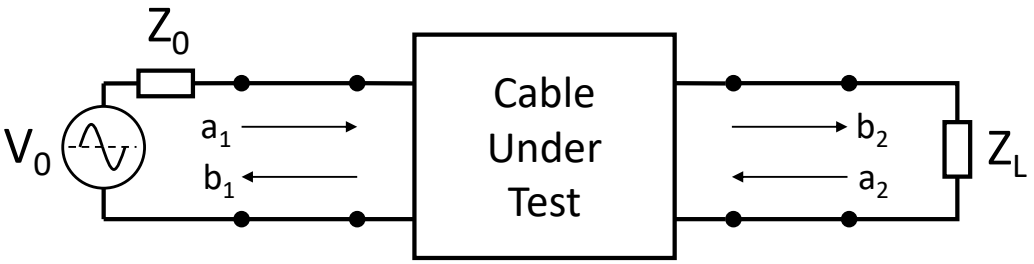

Fig. 5. Two-port model of coaxial transmission line for S-Parameter analysis

One of the chief modes of analysis of the cables under test in this work involves observing their S-parameters, obtained either empirically or through simulation. Each test cable is treated as a two-port network, as shown in Fig. 5. In the case of empirical measurements, the source is supplied by port 1 of a VNA, and the load termination

provided by port 2. In the case of simulation, two ideal ports are simulated, one of which is designated as a source of excitation. In both cases, the source and load ports are matched to the characteristic impedance of the transmission line, which is 75 Ω. The signals present on the line are decomposed into traveling wave amplitudes in opposing directions at each port of the network, with the a_n components traveling towards the network ports, and the b_n components traveling away from them [23]. The relationships between them can be represented in matrix form as follows:

$$\begin{bmatrix} b_1 \\ b_2 \end{bmatrix} = \begin{bmatrix} S_{11} & S_{12} \\ S_{21} & S_{22} \end{bmatrix} \begin{bmatrix} a_1 \\ a_2 \end{bmatrix} \quad (1)$$

However, where the load impedance is equal to the characteristic impedance and no signal is being introduced into port 2 ($a_2 = 0$), this simplifies to:

$$b_1 = S_{11} a_1$$

$$b_2 = S_{21} a_1 \quad (2)$$

Therefore, the remaining, non-zero S-parameters can be expressed as a ratio, which is often given in dB:

$$S_{11} = \frac{b_1}{a_1}$$

$$S_{21} = \frac{b_2}{a_1} \quad (3)$$

An important tool in the evaluation of signal leakage from test cables used in this work stems from the following equality:

$$\sum |b_n|^2 = \sum |a_n|^2 \quad (4)$$

This equality holds for a lossless network. For lossy networks, the following would be true:

$$\sum|b_{\mathrm{n}}|^2 < \sum|a_{\mathrm{n}}|^2$$

$$\sum|b_{\mathrm{n}}|^2 = \sum|a_{\mathrm{n}}|^2 - P_{Loss} \tag{5}$$

The losses in the cases studied would be either dissipative losses in the transmission line (or test-leads, connections etc.), or radiative losses. The dissipative losses given in the cable specifications range from 0.43 dB/100m at 5 MHz to 6.79 dB/100m at 1 GHz [24]. Given test cable lengths of approximately 50cm, the expected dissipative loss would range from 0.002 dB to 0.034 dB, which is to say that they are negligible. Test lead losses are calibrated out of the VNA readings, and there are no such losses in the HFSS model. Equations (3) and (5) can be combined and rearranged to yield power loss in dB relative to the incident power, $|a_1|^2$, and as a function of angular frequency, ω:

$$10\log_{10}[|S_{11}(\omega)|^2 + |S_{21}(\omega)|^2] = P_{Loss}(\omega)\ \mathrm{dB} \tag{6}$$

The expected power loss for an undamaged and properly connected test cable tested in such a manner would therefore be very close to zero, particularly in the frequencies below 50 MHz. This expectation is confirmed for both modeled and measured results and compared to the manufacturer's specifications in Fig. 6. With this very low loss as a baseline, any additional loss observed in a damaged cable could then reasonably be assumed to have been lost to radiation by some mechanism. Likewise, since the network under test does not have any gain, any deviations to the positive side of 0 dB would need to be explained by ingress of some signal external to the system,

which can only arise for the physical measurements, and will be discussed in more detail later. This approach of applying equation (6) to VNA and simulation derived S-parameters to produce plots of the kind shown in Fig. 6 was found to be a useful analysis of test cable properties and is employed throughout chapter 5.

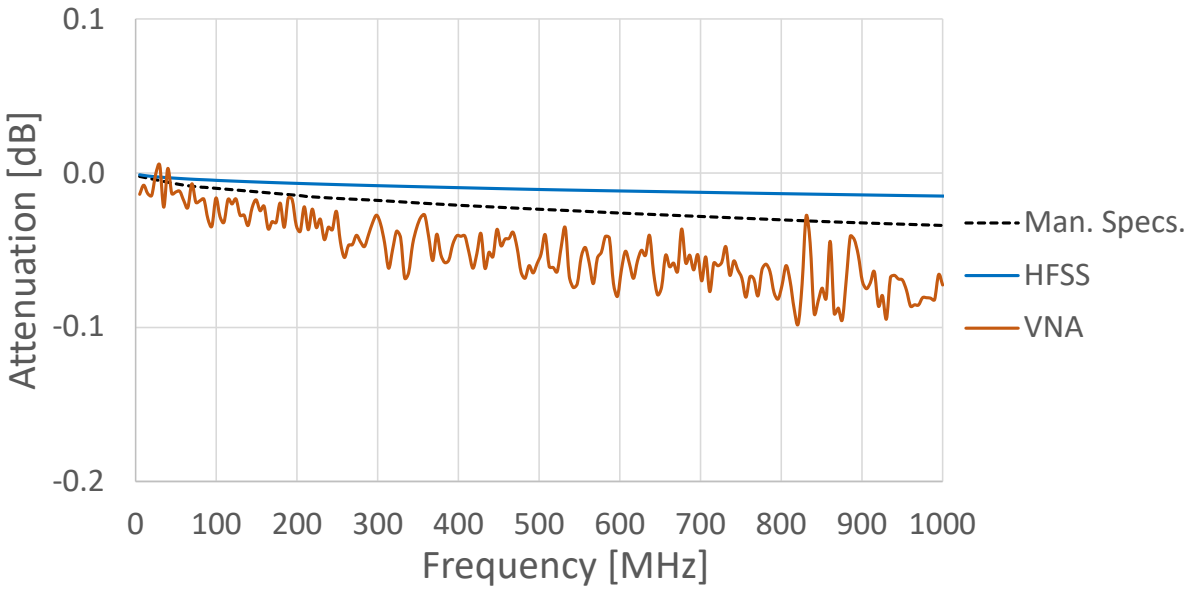

Fig. 6. Attenuation vs. frequency of an undamaged test cable

Before concluding this discussion of S-parameters, there is one note on the S_{11} plots in subsequent sections. Due to a constraint on the available adapters for the cable types under test, type-F connections were used for connecting the test segments to the VNA. These connectors do not have return losses as low as the network cables themselves, and some artifacts of this can be seen in S_{11} of the various S-parameter plots. Since the primary figure of merit produced from the S-parameter readings is the overall signal loss, equation (6), this slightly elevated return loss has a negligible effect on the observations and is unavoidable given the available connectorizations. For

reference, the S-parameters of the test leads connected together with a female-to-female type-F connector are shown in Fig. 7.

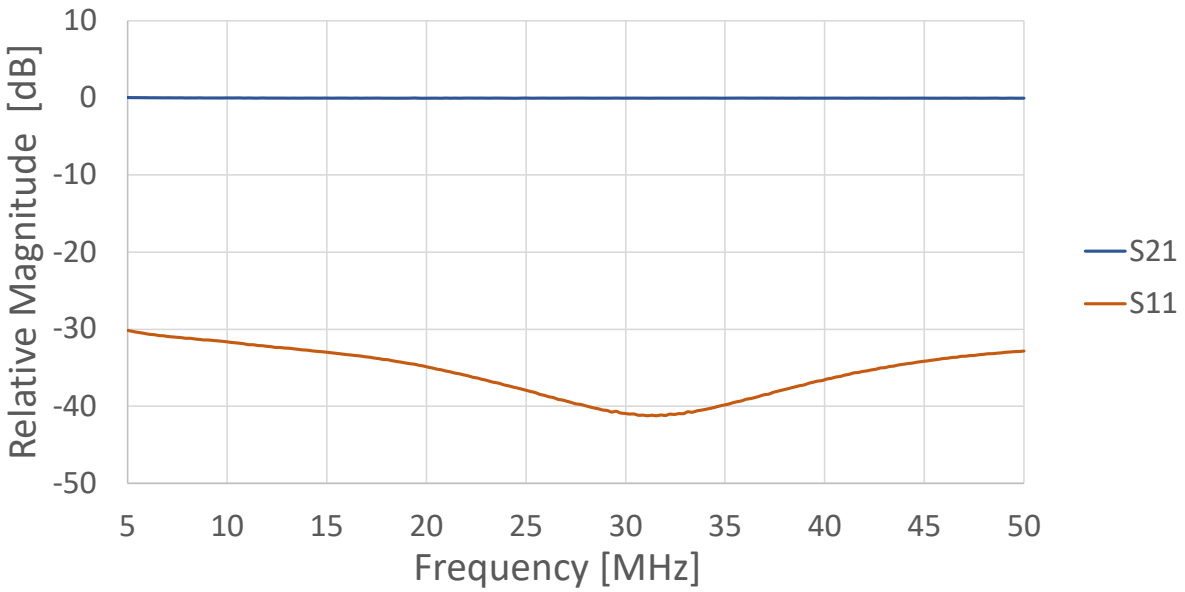

Fig. 7. Loop-connected VNA test lead S-Parameters (type-F connectors)

CHAPTER 3 – EXPERIMENTAL DESIGN

3.1 Coaxial Test Segment Preparation

Sample cables were prepared from a reel of CommScope P3 .625 jacketed coaxial cable, with a characteristic impedance of 75Ω [24]. Specimens were produced at a variety of lengths, both with and without damage to the sheath. One class of sheath fault was produced by lightly scoring then repeatedly flexing the cable until a full radial crack resulted (Fig. 8). In outside-plant (OSP) portions of HFC networks, this type of damage arises from a combination of mechanical stresses due to wind, temperature change, and vibration from nearby traffic, as well as from bending and other manipulations during the installation process. The relative position of the radial crack on the cable segment, as well as the degree of contact between the two resulting sections of sheath conductor were both subject to variation across different samples.

Another type of fault was produced by ablating a section of the sheath with a rotary grinding disc until a rough-edged opening in the sheath was produced. This process was not performed so deeply into the cable as to compromise the center conductor, but, in addition to the sheath, it did remove some portion of dielectric in the affected area (Fig. 9). This emulates cable damage produced by rodents (primarily squirrels) chewing on cables (Fig. 10), and most commonly occurs in cables deployed aerially (i.e., attached to a strength member strung between utility poles), as opposed to the exposed portions of network cables in underground network facilities (e.g., in pedestals, vaults, conduits, etc.).

A summary of the various coaxial test segments produced, along with their relevant parameters appears in Table 1.

Table 1 Coaxial Test Segment Summary

Test Segment	Fault Type	Fault Location	Segment Length	DC Resistance
00	None	-	40 cm	0 Ω
01	Pseudo Squirrel-Damage	7 cm – 27 cm	40 cm	0 Ω
02	Radial Crack w/ Partial Contact	25 cm	50 cm	1.2 Ω
03	Radial Crack – Fully Disjoint	23 cm	50 cm	∞ Ω
04	Radial Crack – Fully Disjoint	15 cm	50 cm	∞ Ω

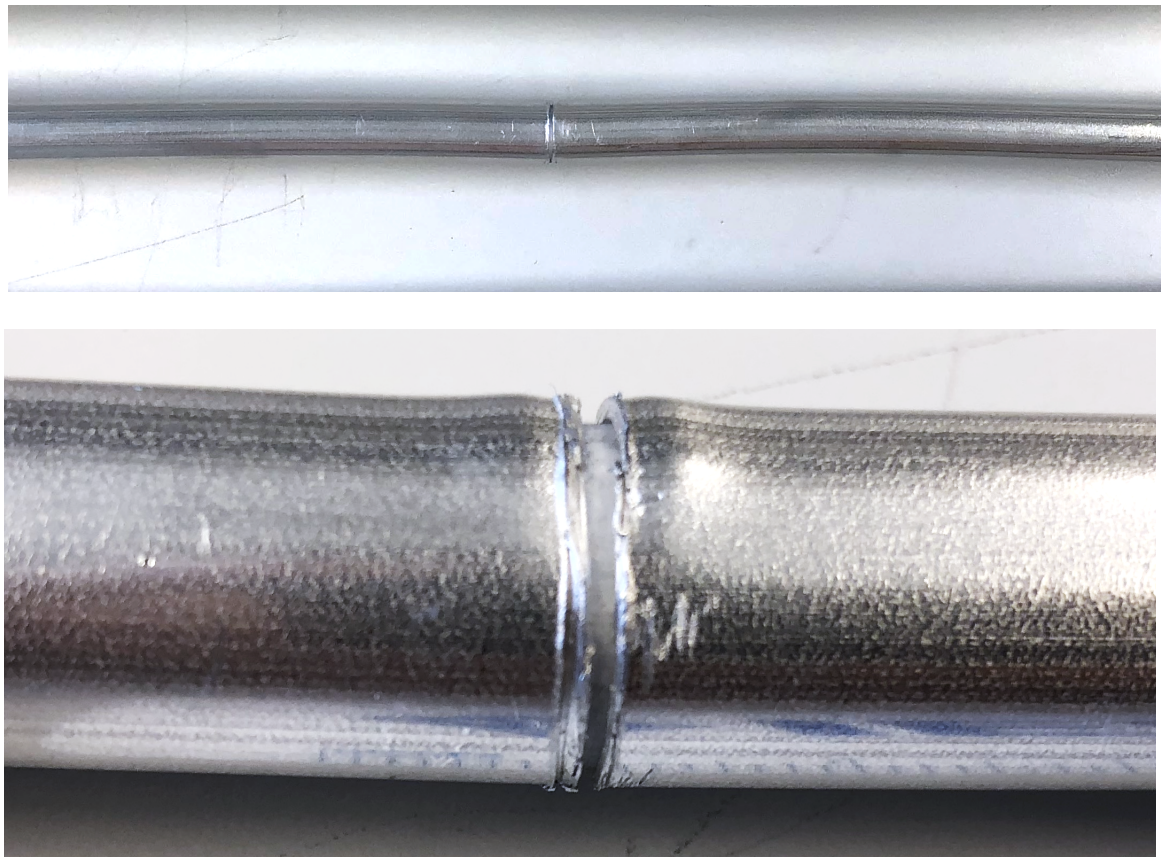

Fig. 8. Radial cracked test cable (enlarged view, bottom)

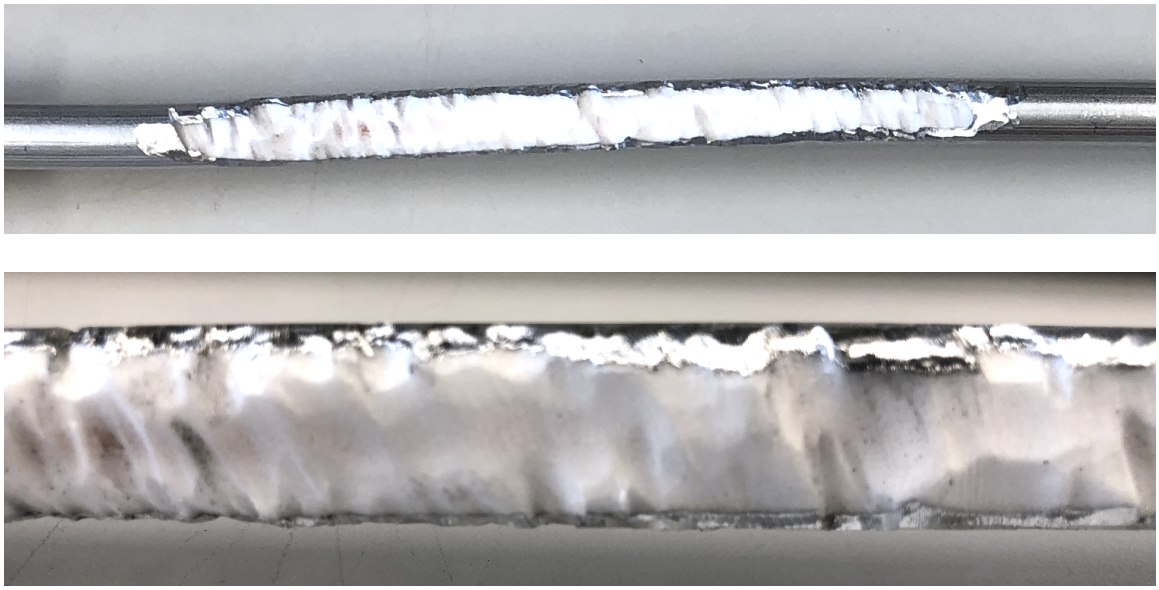

Fig. 9. Simulated squirrel damage (enlarged view, bottom)

Fig. 10. Squirrel-damaged coaxial cable in an HFC network

In the case of test segment 02, the intermittent contact initially made for inconsistent test results as its properties were found to be highly sensitive to the precise physical orientation between the sheath segments on either side of the crack. In order to

stabilize this test sample, the cable was manipulated until it exhibited a strong resonance in the ingress spectrum test, and then splinted with electrically insulated clamps to maintain its orientation for further testing. An ohm-meter then read a DC sheath resistance of approximately 1.2 Ω, as noted in Table 1.

In the case of samples 03 and 04, the radial crack was generated in the same method used for 02, detailed above, but the cracked cable was manipulated until a gap of approximately 1mm was present between the two, now fully disjoint, sections of sheath conductor. Any small fragments of the aluminum conductor that might act to bridge the gap were removed, and sheath discontinuity was verified using an ohm-meter.

Fig. 11. Test cable segments 00 – 04 (top to bottom)

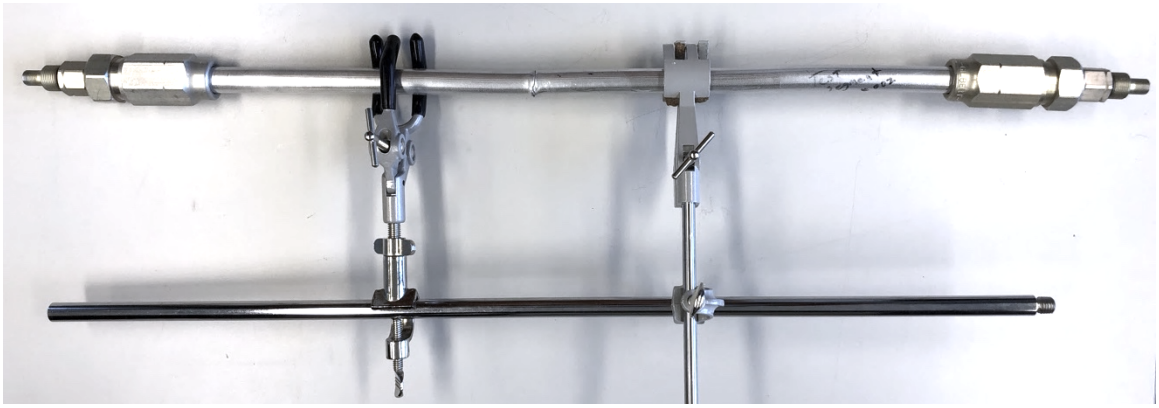

Fig. 12. Test cable segment 02, splinted for stability with insulated clamps

3.2 Ambient Ingress Spectrum Assessment

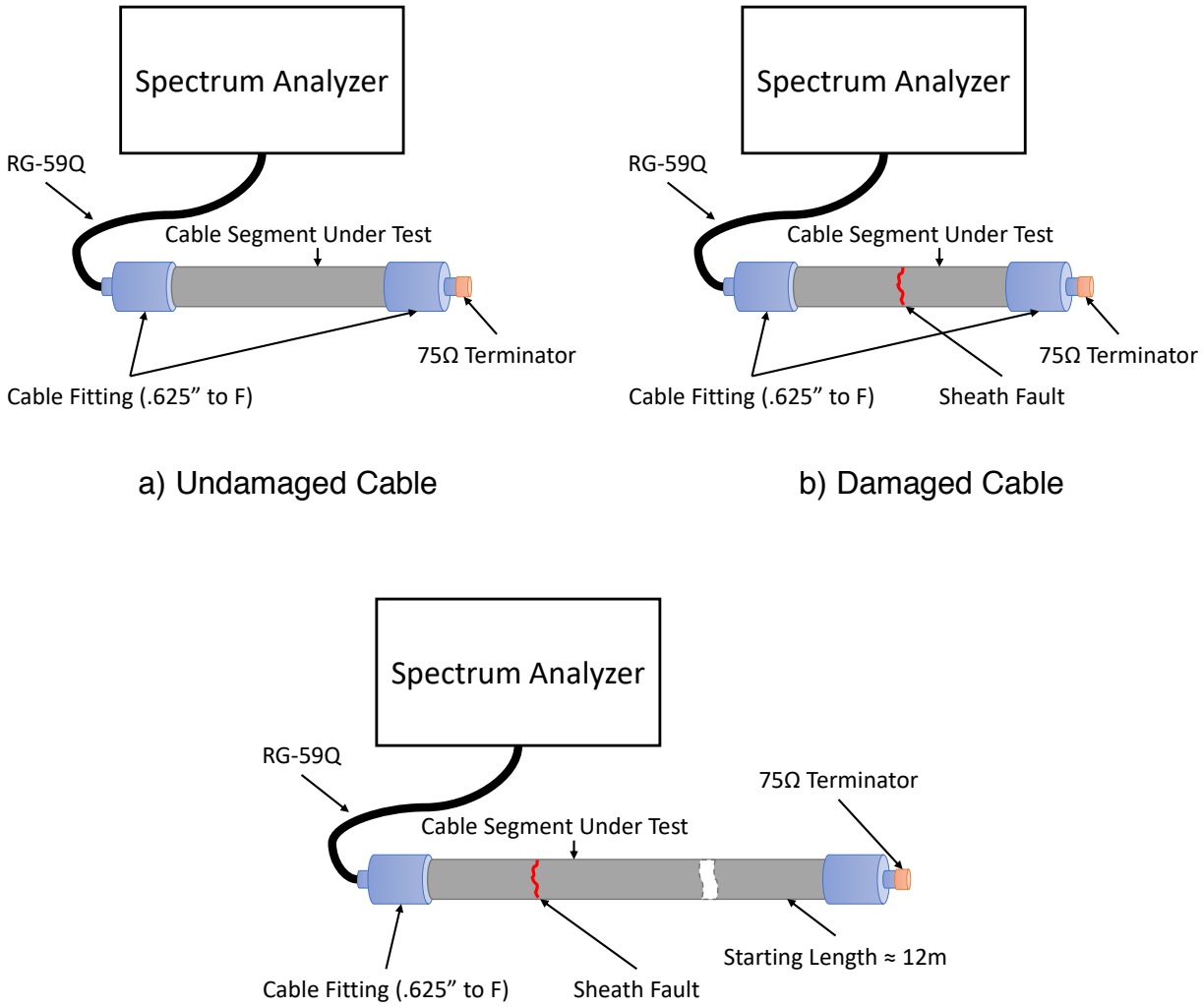

a) Undamaged Cable

b) Damaged Cable

c) Progressively Shortened Cable

Fig. 13. Ambient signal ingress test setup

Test segments prepared as above were terminated with female-to-female connectors, one side of which was a 75Ω Type-F jack, and the other of which was

designed to fit the .625” cable (Fig. 11). One test performed was concerned with measuring whether ambient signals in the 5-50MHz range were present on the test cables in the form of ingress. The motivation for this was to ensure that lab generated test cables exhibited receptive properties consistent with real-world sheath faults previously observed in HFC networks and known to introduce ingress signals [2, 3].

To achieve this, one end of a test segment was terminated with a 75Ω type-F terminator, and the other was connected to an Agilent CXA N900A spectrum analyzer (Fig. 13). In the ideal case and with undamaged cable, the system thus constructed should be completely closed, and no ingress signals should be detected (Fig. 13a). Such signals are typically present, particularly in the 5-20MHz range [3], so the absence of them in the spectrum analyzer readings generally implies good shielding. Conversely, presence of energy in this band would positively indicate that a test segment exhibited resonance in the band of interest and should therefore be a suitable proxy for real-world sheath faults (Fig. 13b).

3.3 Effect of Cable Length or Termination on Ambient Ingress Reception

Several preliminary tests were performed to validate the hypotheses that relatively short segments of cable would be valid candidates for study. In one scenario, a radial crack fault was introduced onto a long length of cable (approximately 12 meters), and its spectrum confirmed the presence of ingress. The cable length was then progressively shortened (from the end distal to the radial crack), and the ingress observation repeated in several iterations until the cable was 50cm in length (Fig. 13c). At this final length, one

such specimen became test cable 02. Results of the ingress spectrum for this specimen at two disparate lengths are shown in Fig. 15. This was not meant to be a detailed assessment of the effects of cable length, nor to eliminate it as a parameter of interest, as the ingress measurements are not calibrated and vary substantially with time and subtle repositioning of the test cable. However, the results were sufficient to support the conclusion that the much more convenient 50cm length would be appropriate for further testing. Later tests, discussed in chapter 3, look in more detail as to the effects of cable length. Similarly, variations in cable termination methods were explored to see if these would have substantial impact on the observed behavior. These were drawn from typical connectorization and termination equipment common to HFC networks (Fig. 14). It was found that this variable did not have a significant impact, and so subsequent tests focused on test segments with straightforward cable termination.

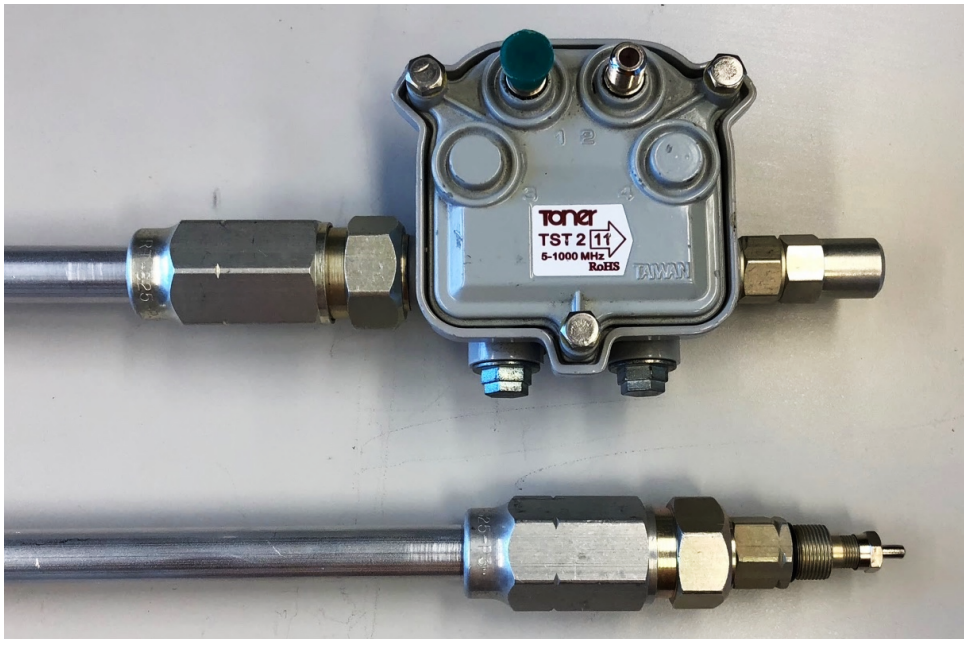

Fig. 14. Various Cable Segment Terminations Tested

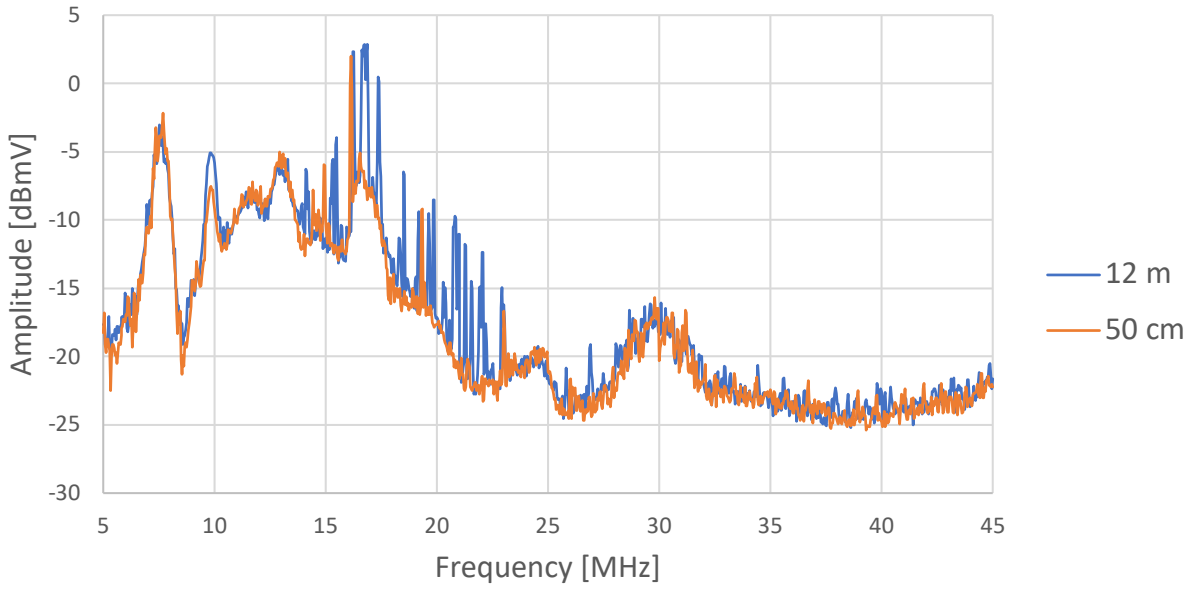

Fig. 15. Test Segment 02 Ingress Spectrum at Different Lengths

3.4 Reflection and Transmission Testing

A second class of test was performed whereby cable segments were connected in a through-test configuration to a vector network analyzer (VNA) (Fig. 16). These tests measured the reflected power (S_{11}) and transmitted power (S_{21}) as a function of frequency over the range of 5 to 50MHz or 5MHz to 1GHz. Further analysis on the data thus obtained was performed to show the total loss of the system. For the ideal, undamaged cable case this should be conservative of the power produce by the VNA (assuming no resistive losses), such that:

$$10\log_{10}[|S_{11}(\omega)|^2 + |S_{21}(\omega)|^2] = 0\text{dB},\ \forall\ \omega \qquad (7)$$

Since resistive losses are negligible for the test segments used (generally on the order of 50cm in length), any deviation from this ideal would represent power radiated

from the cable under test (egress), or power picked up by the cable from ambient sources (ingress) [24]. As such, this metric provides a reliable indicator of a test cable's radiative properties as a function of frequency.

For the control VNA test, an undamaged cable (test segment 00) was used (Fig. 16a). Various damaged specimens (test segments 01-04) were likewise connected (Fig. 16b). Where the sheath fault was not centered on the test segment, as in test cable 04, VNA measurements were taken both with the fault closer to the source and, alternately closer to the receive side of the VNA. This permutation was conducted to ascertain whether relative fault position on a cable would be a meaningful determinant of the radiative properties of a test segment, for similar motivations as discussed above regarding ambient ingress spectrum assessment.

Given that common-mode currents are hypothesized to play a significant role in producing the observed radiative phenomena, another variation on the basic VNA test was performed where damaged cable segments were connected as before to the VNA, but with the addition of ferrite beads around the cable diameter (Fig. 16c). This was done to increase the effective choking impedance that any common-mode currents would encounter. If any common-mode currents do exist on a cable, then the above hypothesis would predict that suppressing them should in turn have a measurable effect on the VNA measurements, and this configuration is intended to test that prediction. Results of test cables with and without ferrite beads are compared to determine if an observable change in radiative properties occurred as a result of the adding the ferrite beads. A mixture of

type 43 and type 31 ferrites was used, with total of 10 beads in all. The ferrite types were selected for their resistive loss in the bandwidth of primary interest, i.e., 5 to 50MHz.

Given the principal of reciprocity, test segments that demonstrate radiative coupling in the bandwidth of interest, e.g. in the ambient ingress test, will perform equally well at transmission and reception in that band. Since the power budget calculation from equation (7) would take into account any of the VNA's source power lost to radiation, as well as any additional power accumulated through ambient ingress at those frequencies, another permutation of the VNA test was executed where the entire test setup was installed inside an anechoic chamber in order to isolate these two effects (Fig. 16d). Measurements thus produced should only show negative deviations, if any, from the ideal case of 0dB as a function of frequency.

Another series of tests were performed where the test segments were attached to a longer section of undamaged cable (approximately 12m), with a commonly used connector design to splice 0.625" cables. This longer cable assembly was then connected to the VNA in a through configuration, as illustrated in Fig. 16e. Measurements for various test segments so incorporated were taken with the VNA source connected to the end near the fault, and also with the source connected to the end far from the fault. The motivation for this was to test for the effects of overall cable length and fault position on the radiative properties of the cable segments under test. Lastly, ferrite beads were applied to the longer composite cable assembly under test, combining the configurations of Fig. 16c and Fig. 16e.

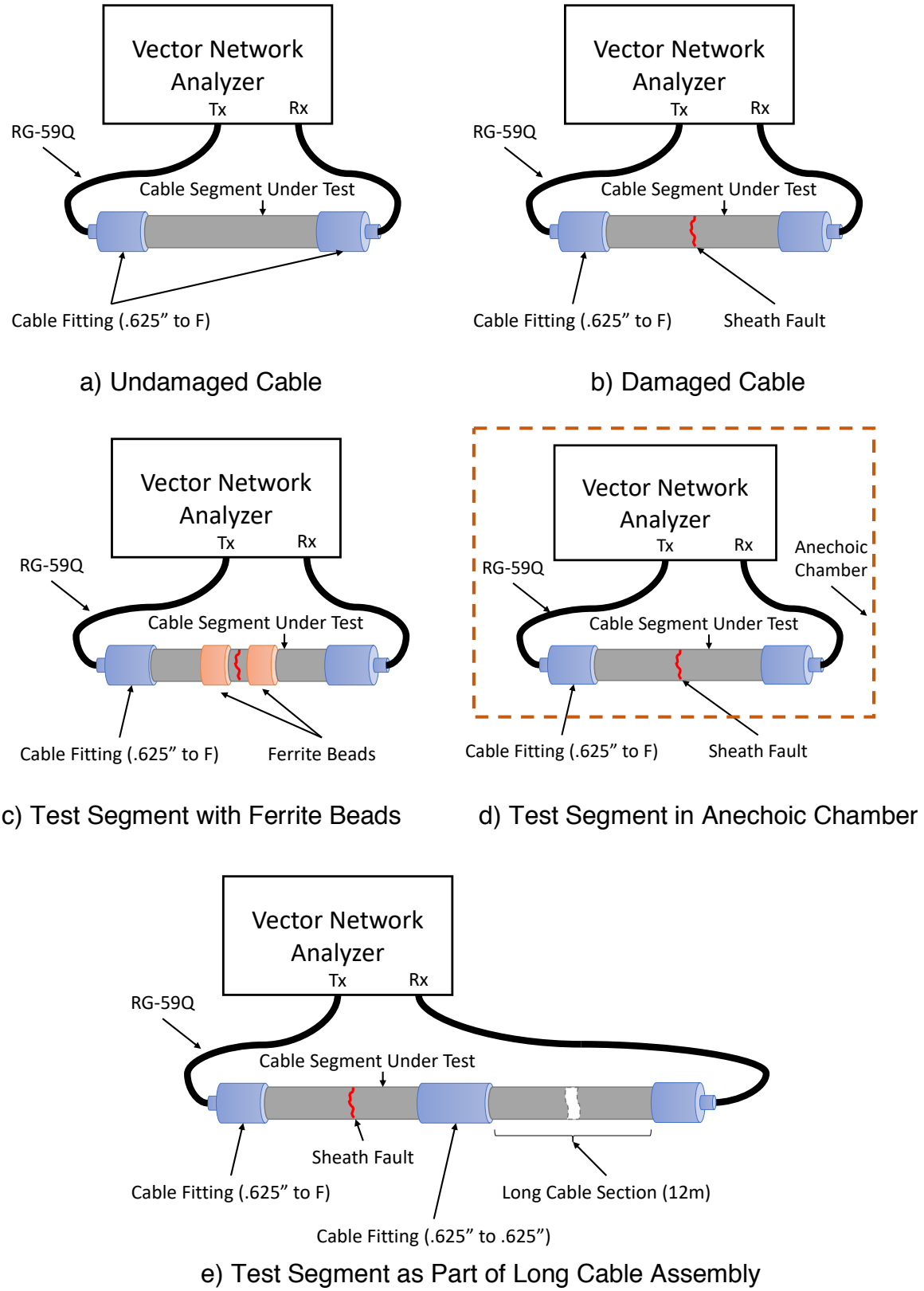

Fig. 16. Reflection and transmission test setup (S_{11} and S_{21})

CHAPTER 4 – SIMULATION

Models of the various physical test cables listed in Table 1 were generated using the HFSS electromagnetic field simulation package [12]. The goal of the simulation was to reproduce, if possible, the observed physical characteristics of the test cables, including reflectance, transmission, and radiative properties. If shown to be consistent with measurable properties of the cables, the models may then be suitable to explore features such as electric field magnitude and orientation or current distributions, that would be difficult to measure directly.

4.1 Undamaged Cable

The baseline simulation was of a 50cm length of undamaged coaxial cable (Fig. 17). The physical properties, such as material, thickness/diameter of conductors, relative permittivity, etc., were derived from the manufacturer's specifications [24], as summarized in Table 2. Details of the calculations relating to test cable parameters are given in Appendix A. Ports were simulated on either end of the cable, with one being configured as the source of excitation. Parameters including impedance, S_{11}, and S_{21}, all as a function of frequency, were recorded from the simulation, as were H or E field intensities at various locations of interest.

Table 2 Commscope P3 0.625 Cable Specifications

Property	**Value**
Outer Conductor, Outer Diameter	15.875 mm
Outer Conductor Thickness	0.7620 mm
Outer Conductor Material	Aluminum
Inner Conductor, Outer Diameter	3.480 mm
Inner Conductor Material	Copper-Clad Aluminum
Dielectric Material	Polyethylene Foam
Dielectric Relative Permittivity	1.38
Characteristic Impedance	75 Ω
Structural Return Loss	30 dB @ 5-1002 MHz
DC Resistance, Inner Conductor	2.8 Ω/km
DC Resistance, Outer Conductor	0.85 Ω/km

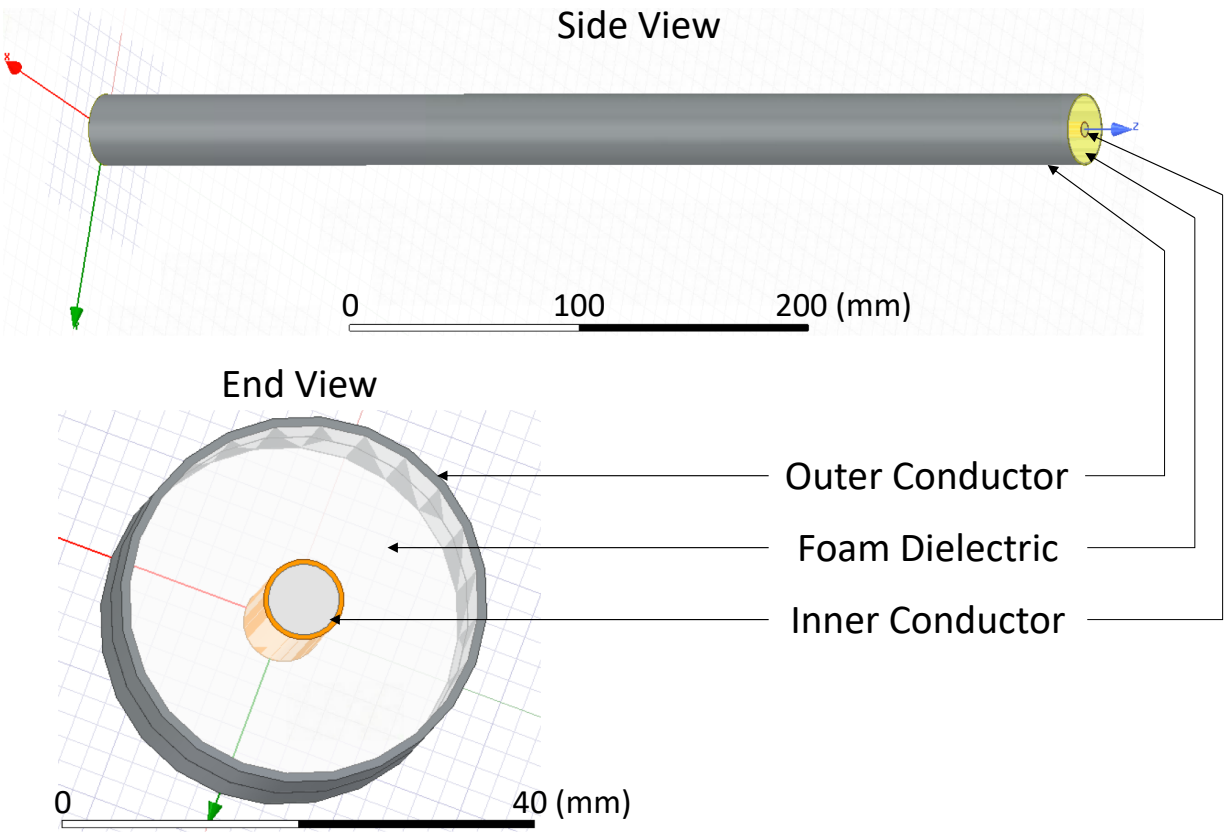

Fig. 17. Model of undamaged cable in HFSS

4.2 Squirrel-damaged Cable

In general, damaged cables were simulated by subtracting various geometries from the undamaged cable model components. In the case of squirrel damage, discs were modeled with edge profiles approximating those of a squirrel's upper and lower pairs of incisors, and with radii producing arc profiles similar to the bite pattern thereof. These were then overlapped with the modeled cable to varying depths, and the overlapping region subtracted from the cable model. The depth of penetration was parameterized in the model, but, as with the physical test samples, the depth was never such that the center conductor was compromised, although dielectric material was removed in addition to sheath. An example of this can be seen in Fig. 18.

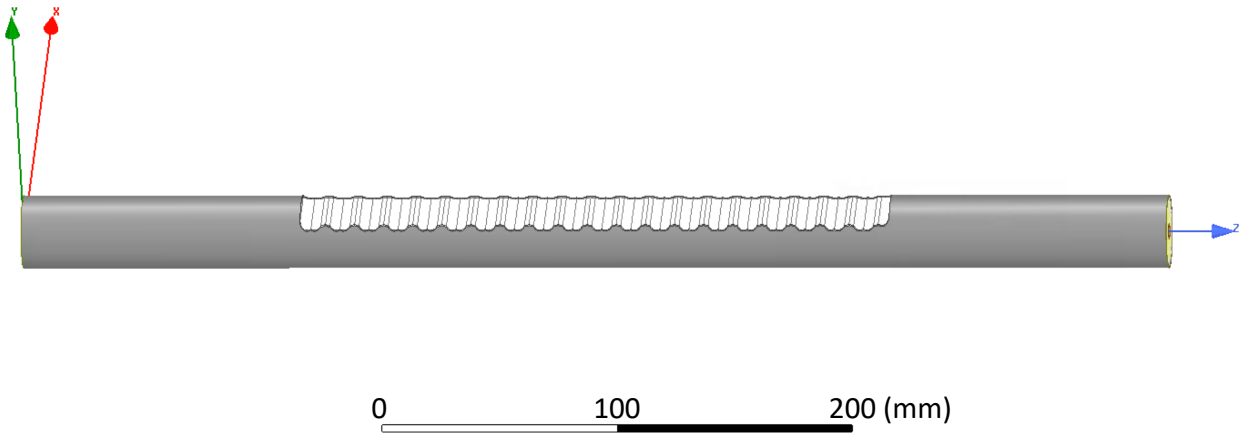

Fig. 18. Model of squirrel-damaged cable in HFSS

4.3 Fully Disjoint Radial Crack

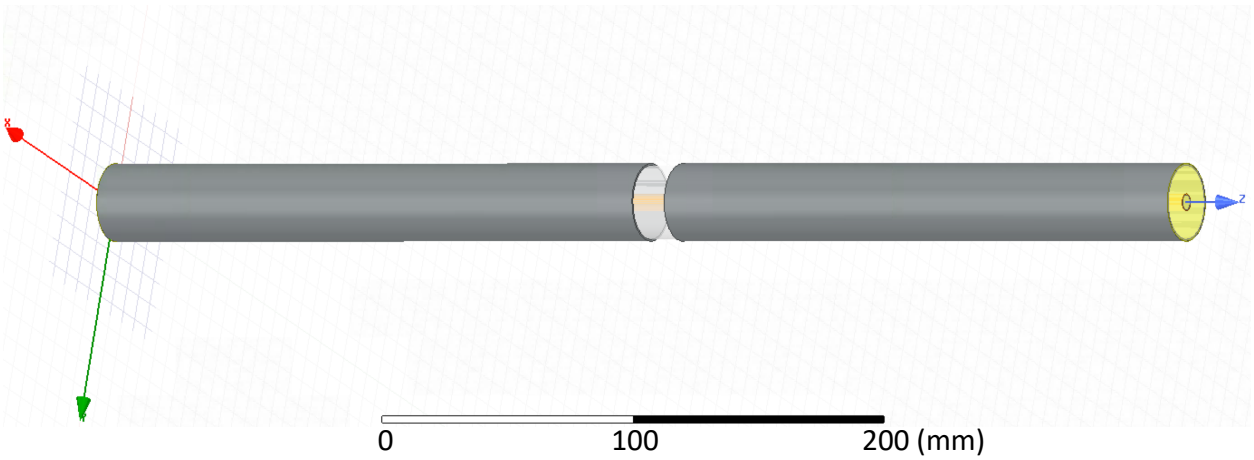

Fig. 19. Radial crack model in HFSS

For the radial crack case, an annular ring of varying width was subtracted from the model cable's sheath element only (the dielectric and other elements remained intact), as illustrated in Fig. 19. The width of the removed sheath material was parameterized (dimension *h* in Fig. 20.) to facilitate modeling a range of values for this variable. The value for *h* used in simulations was generally between 0 (i.e., no damage) and 1 mm (although Fig. 20 depicts a 15 mm gap for illustrative clarity). In addition to the results mentioned above, current distributions and electromagnetic fields were analyzed via the model.

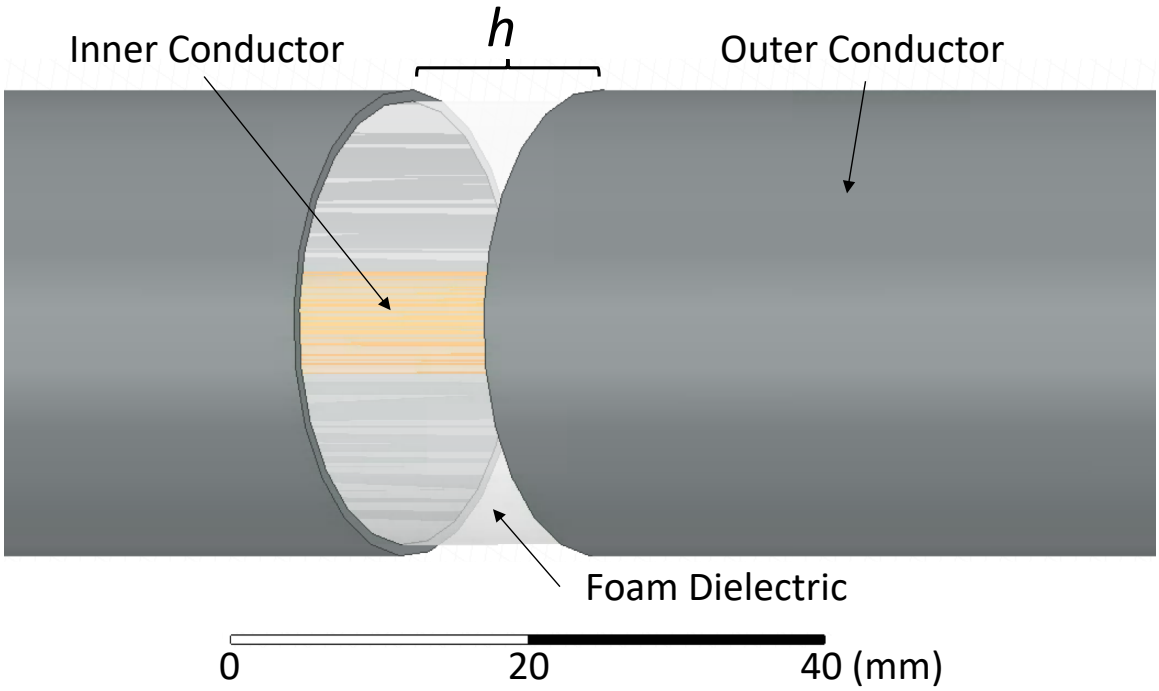

Fig. 20. Radial crack model in HFSS, enlarged

4.4 Bridged Radial Crack Bridge

In many real-world cases, it often happens that the two sections of sheath conductor on either side of a radial crack are physically disjoint but maintain some degree of electrical contact. To model this scenario, a strip of the outer sheath is left in place when subtracting what would otherwise be a complete annular ring from the sheath conductor (Fig. 21). As with the fully disjoint case, the width of the gap is parameterized, but in addition, the arc angle of the remaining portion of the sheath in the gap region is also parameterized (h and θ, respectively, in Fig. 22). For clarity, the bridged gap on the left of Fig. 22 reflects h = 15 mm, and θ = 20°, whereas the gap on the right is representative of the gap dimensions used for the actual simulations, where h = 1 mm,

and θ could range from 0.05° (depicted) to as much as 10°. Recorded observations for this case are of the same sort as those for the unbridged radial crack case detailed above.

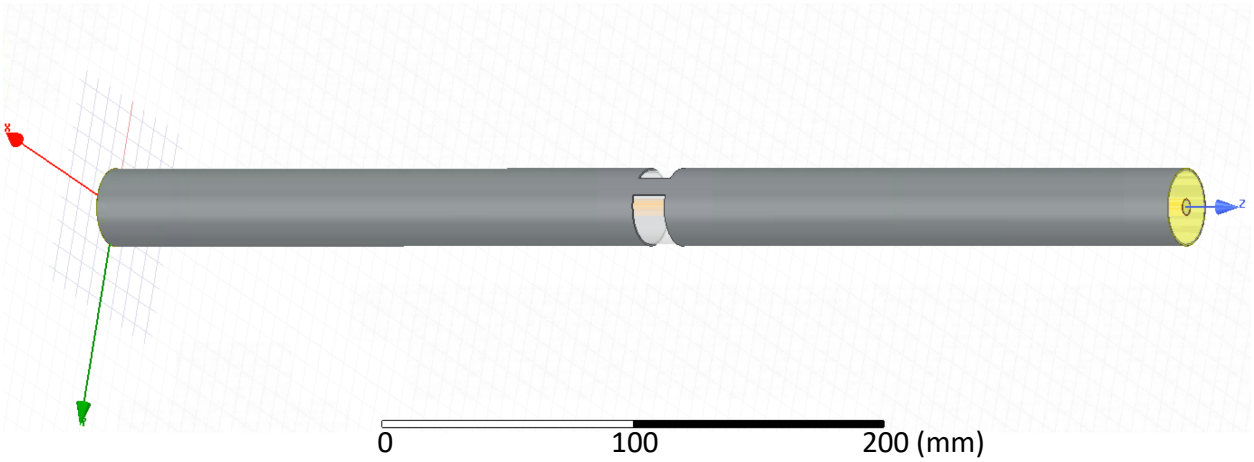

Fig. 21. Bridged radial crack model in HFSS

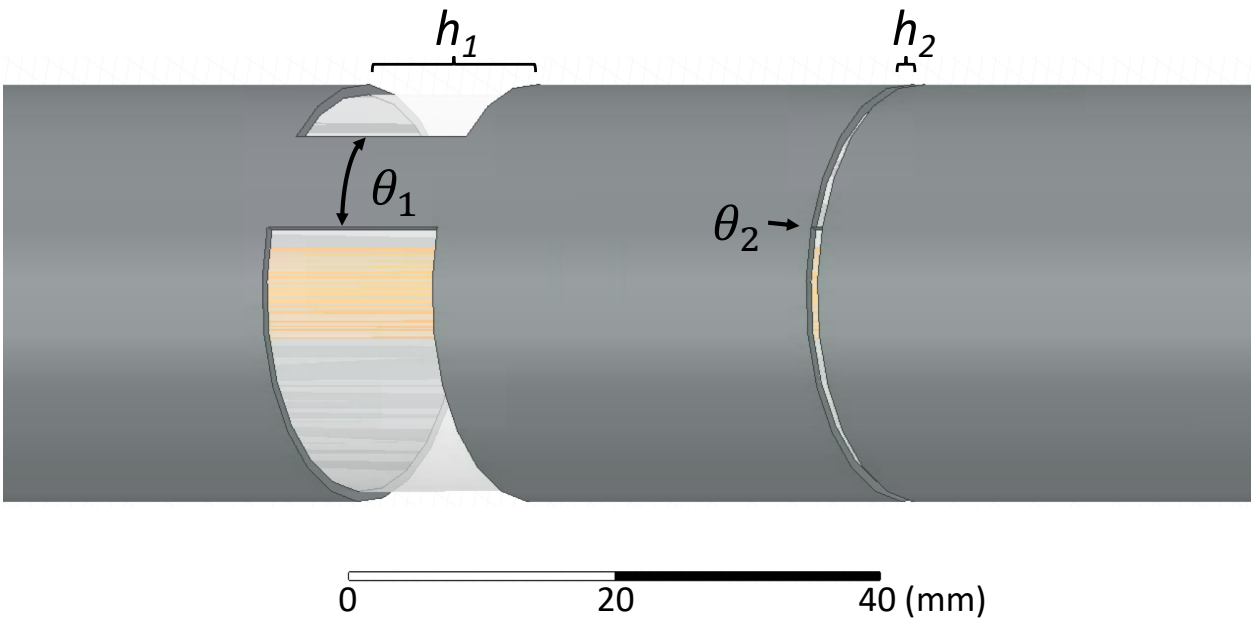

Fig. 22. Enlarged View of Modeled Radial Sheath Gaps with Resistive Bridges

CHAPTER 5 – RESULTS AND CONCLUSIONS

5.1 Control Test – Undamaged Cable

An intact coaxial transmission line can be represented by a lumped element model, as in Fig. 23, where the cable segment in question is arbitrarily being divided into two sections, each with characteristic impedance Z_0, and connected to a source at one end, and terminated by a load at the other. L_0 and C_0 represent the nominal inductance and shunt capacitance of the transmission line. R_{IC} is the resistance per unit length of the inner conductor, while R_{OC} is the resistance per unit length of the outer conductor. The load impedance is Z_0, where

$$Z_0 = Z_A = Z_B = 75\Omega \quad (2)$$

In this case, we would not expect to see any ingress into or radiation from the cable, nor does any opportunity for common-mode currents present itself. This model is used as the baseline for damaged cables in the analysis that follows.

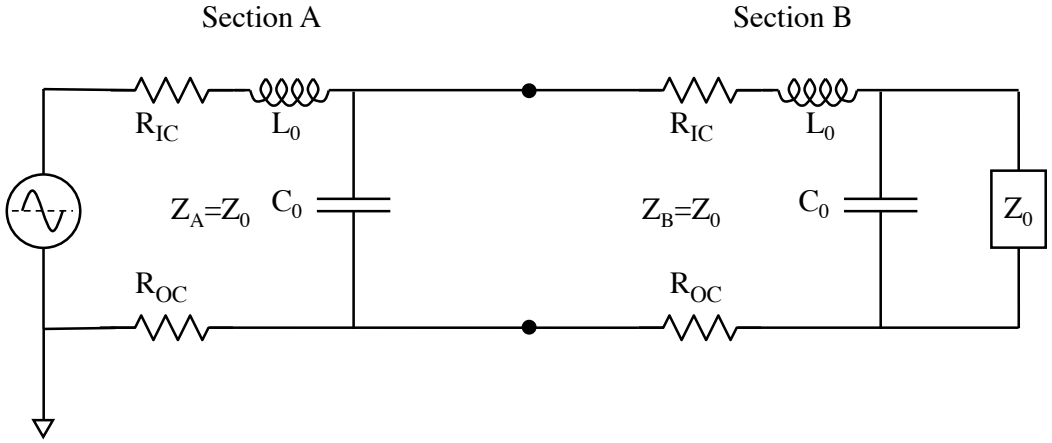

Fig. 23. Lumped element model of intact coaxial transmission line

Accordingly, the spectrum analysis of the undamaged cable (Fig. 24) showed no detectable ingress energy (spectrum of a damaged cable shown for reference), which is as expected for a properly shielded system of the sort implemented by the test setup, and which is representative of a properly installed and undamaged real-world HFC network under ideal conditions. Additionally, the measurements of return loss (S_{11}) and transmission (S_{21}) properties performed on the VNA (Fig. 26) and the HFSS derived values for impedance (Fig. 25) were consistent with the manufacturer's specifications [24]. The values of S_{11} and S_{21} from HFSS closely agreed with the VNA measurements of the physical specimen, as illustrated in Fig. 26, notwithstanding the signature of type-F connectors present in the S_{11} trace, as previously noted. Unsurprisingly, the power budget for the undamaged cable sums almost perfectly to 0 dB (Fig. 27), with only a very slight attenuation showing as the frequency approaches 1 GHz, which is easily explained by increased resistive losses as skin depth decreases. The HFSS model of the cable (Fig. 28 and Fig. 29) shows an absence of H field exterior to the cable, indicating an absence of common-mode currents there.

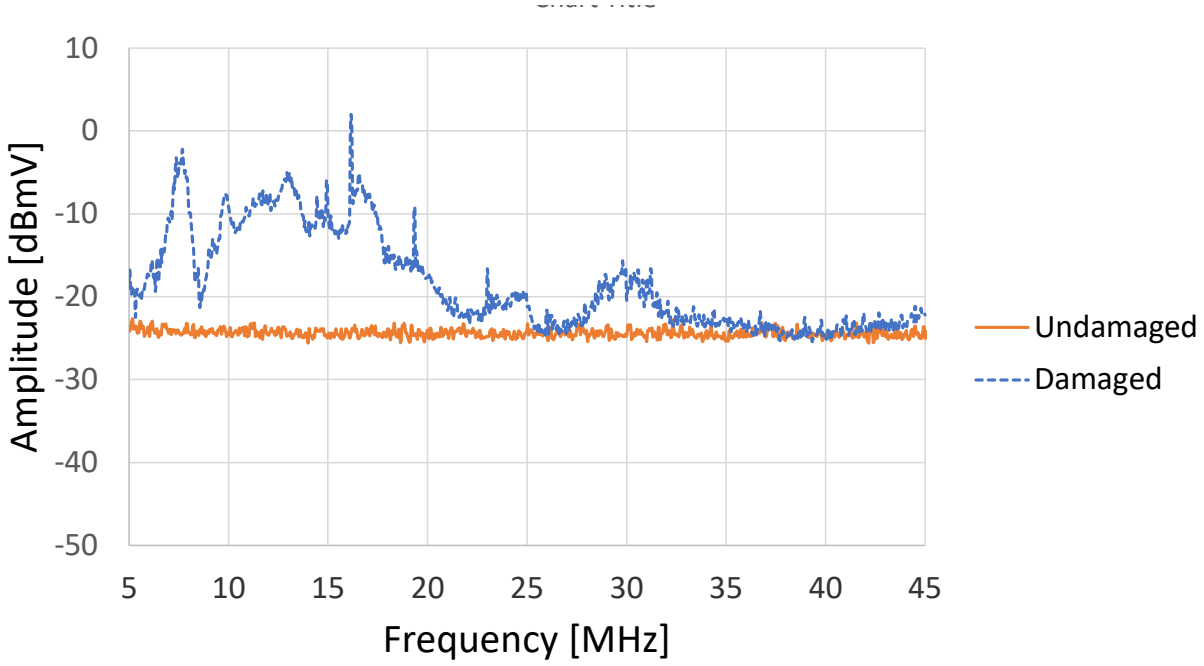

Fig. 24. Ingress spectrum (5-50MHz) of undamaged cable

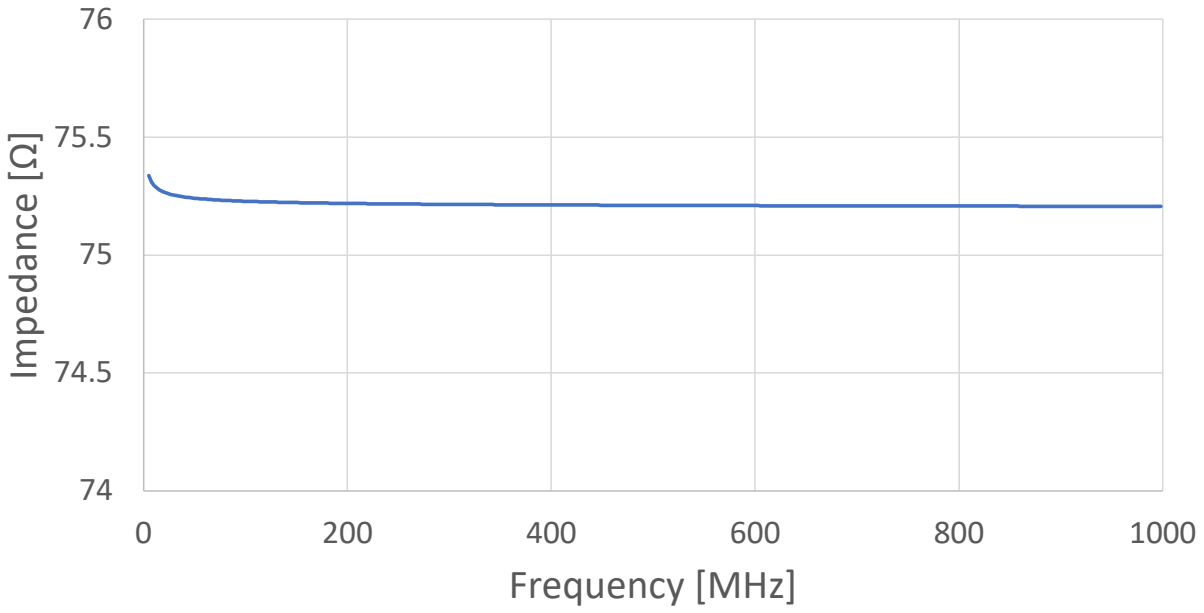

Fig. 25. Impedance vs. frequency of undamaged cable model

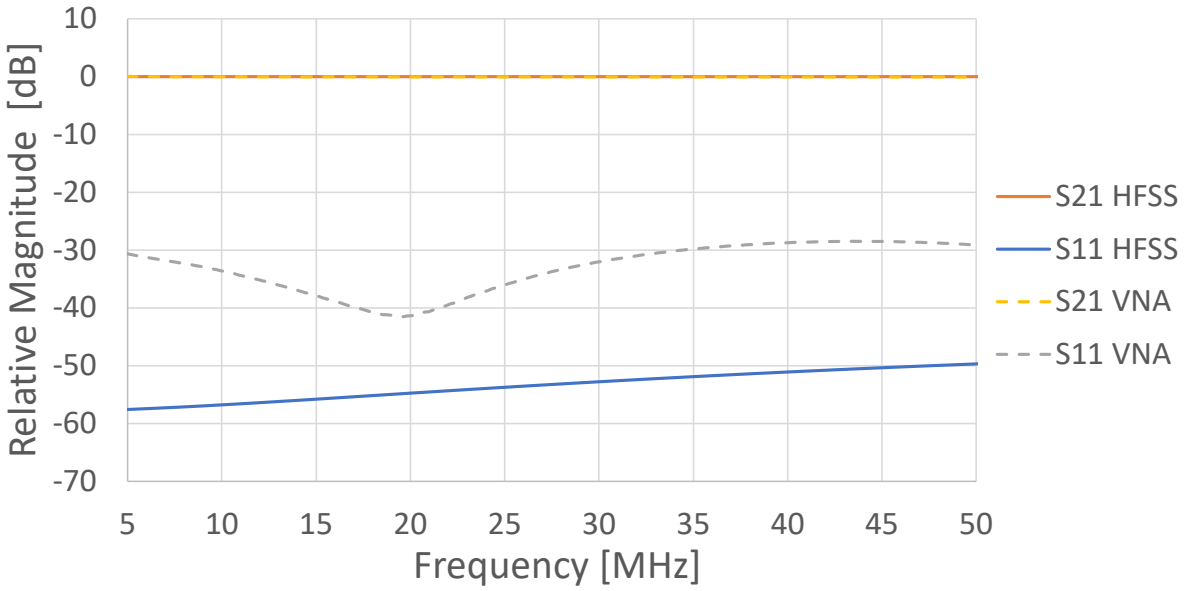

Fig. 26. Modeled and measured S-parameters of undamaged cable (test cable 00)

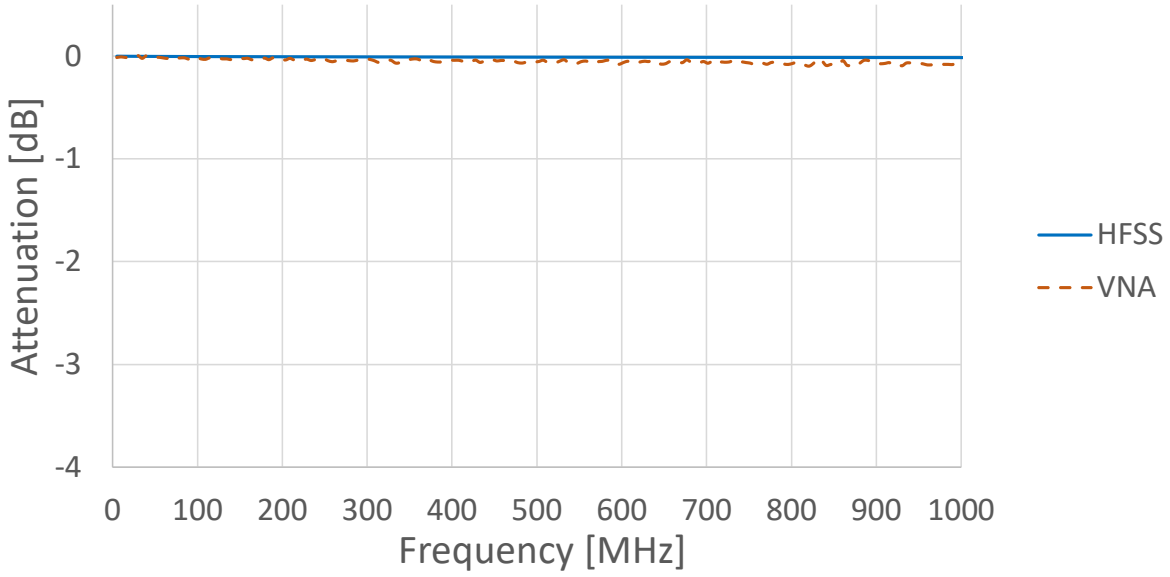

Fig. 27. Power Budget of Undamaged Cable

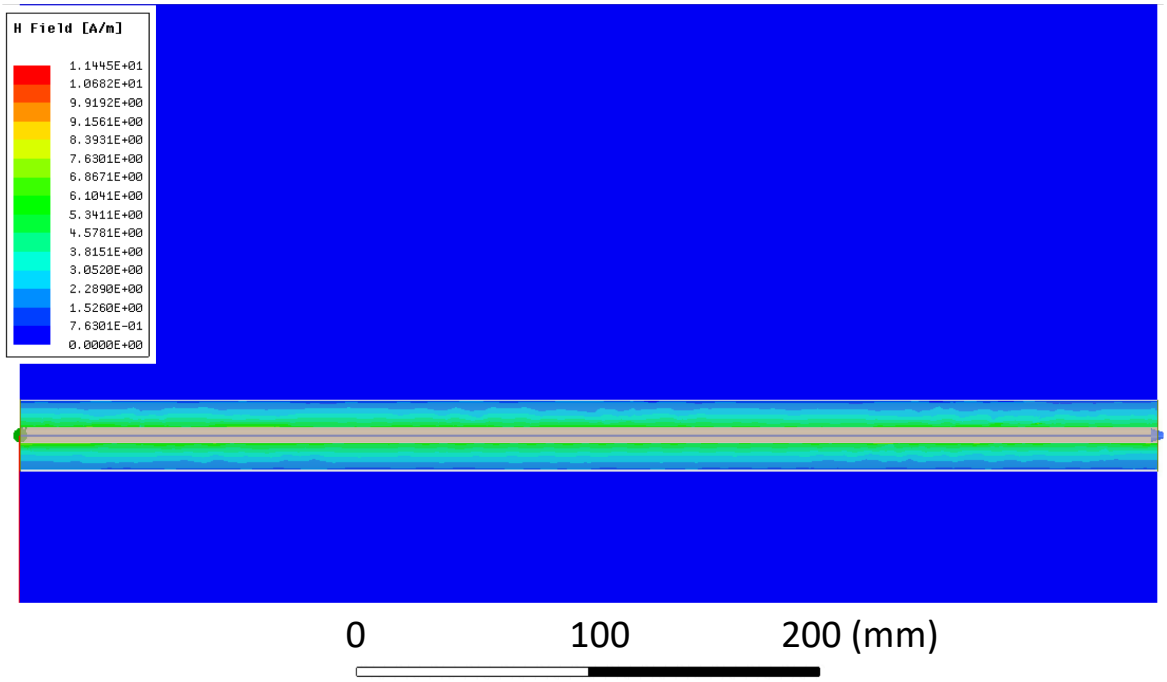

Fig. 28. Simulation of H field lateral section of undamaged cable

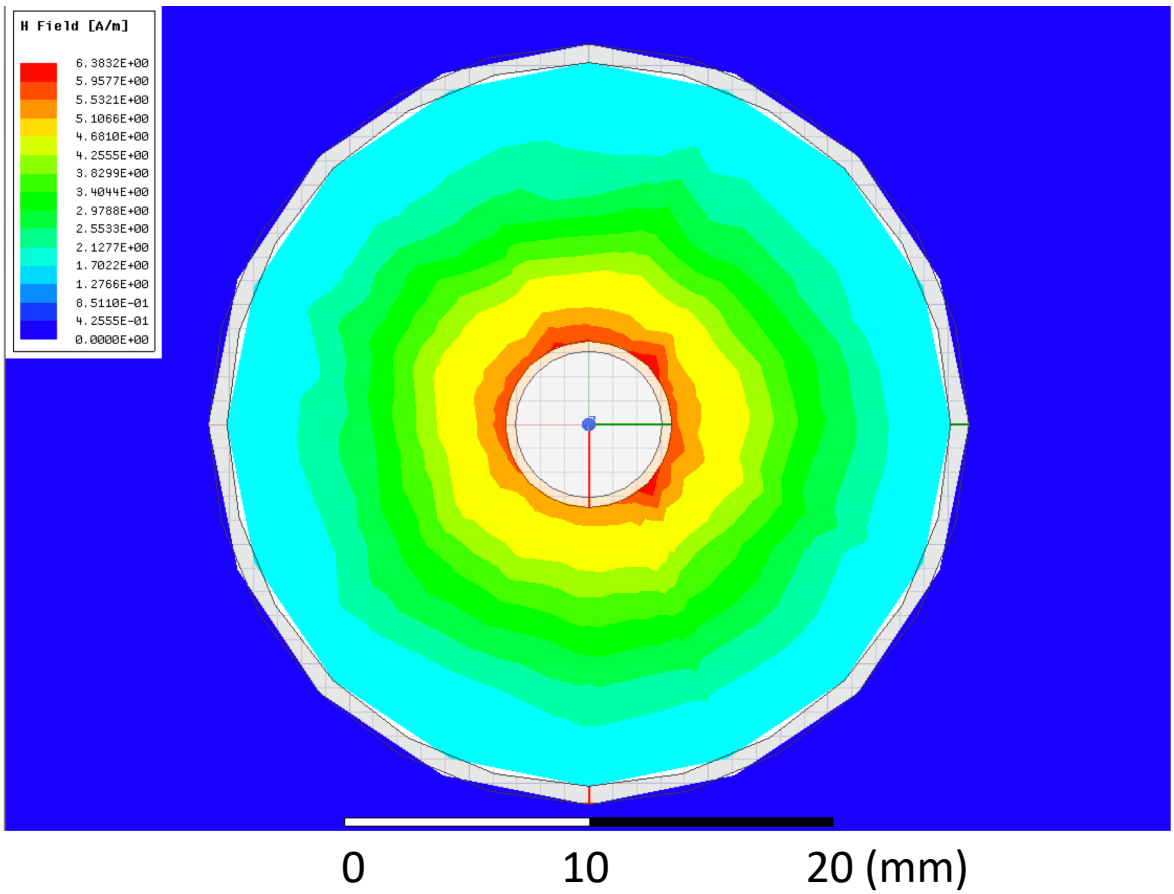

Fig. 29. Simulation of H field cross-section of undamaged cable

5.2 Squirrel-damaged Cable

The pseudo squirrel-damaged cable samples produced did not demonstrate radiative coupling, despite such cases having been observed in real-world examples of squirrel-damaged network cables *in situ*. The agreement between physical measurements and model-derived parameters held for this case as well, however. In both VNA and HFSS data, the principal effect of the squirrel damage was to modestly elevate the return loss (S_{11}) of the damaged cable, as shown in Fig. 30.

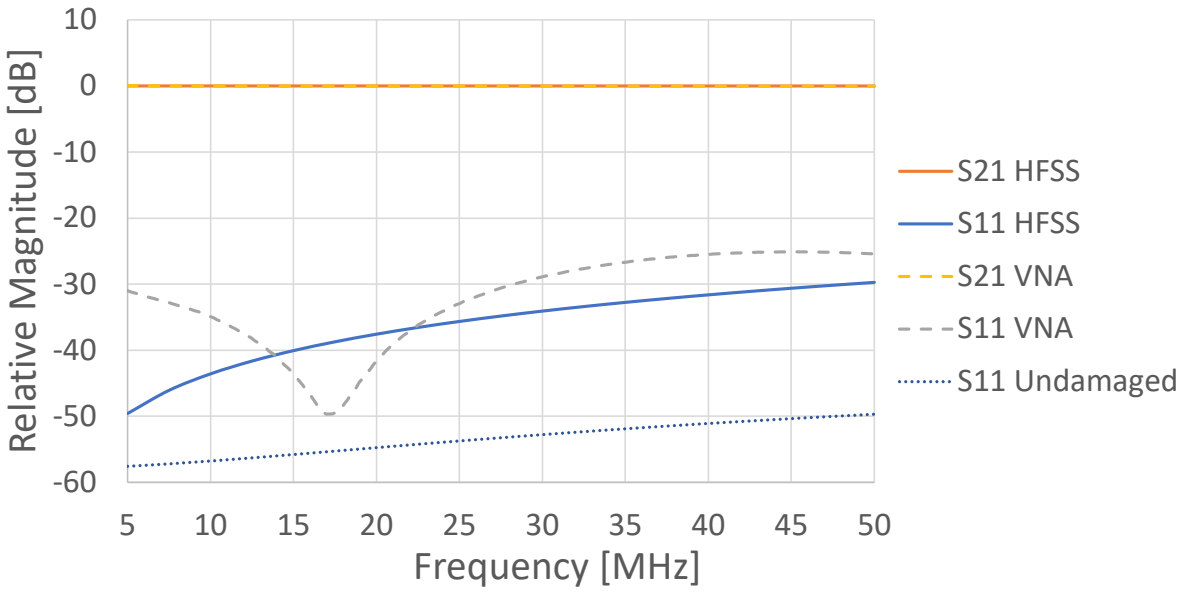

Fig. 30. S-parameters of pseudo squirrel-damaged cable

This is consistent with an assessment of reflection coefficients of various sheath fault geometries found by Cerri *et al* [13] and Manet *et al* [9]. As is illustrated in the lumped element representation of the squirrel-damaged cable (Fig. 31), it would be expected that

the shunt capacitance, C_{Fault}, would be reduced relative to undamaged cables, and that R_{Fault} would be greater than R_{OC}, if only by a small amount in absolute terms given R_{OC}'s very low nominal value per meter [9]. Cerri *et al* found that damage to the cable of this sort would be expected to add some additional effective series inductance, making L_{Fault} greater than nominal (L_{A} and L_{B}) [13]. In all, these deviations from nominal cause a modest impedance mismatch, which is the cause of the increased return loss.

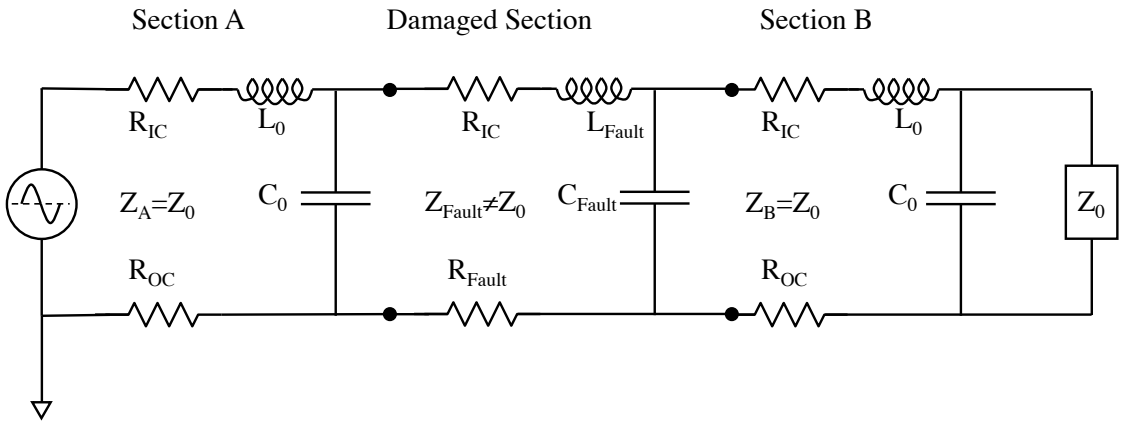

Fig. 31. Lumped element model of squirrel-damaged coaxial transmission line

No detectable ingress energy was observed in the spectrum analyzer test for the frequencies of interest, making the results for this test indistinguishable from those of the undamaged cable. Similarly, the power budget was essentially indistinguishable from the undamaged cable in the primary band of interest (Fig. 32), indicating that the simulated squirrel-damage did not cause significant ingress or egress in the band of interest.

These results are perhaps surprising, given the extent of the damage done to the cable, but from an aperture perspective the damaged sheath section is still much smaller

than the wavelengths in question for the 5 to 42 MHz band. As the frequency of excitation approaches 1 GHz, however, the damaged section's length becomes a sizeable fraction of the wavelength, which is on the order of 30 cm in this frequency range, and accordingly a modest amount of radiative loss is observed in the modeled and empirical results (Fig. 33). These losses can be explained by any of several well-established principles and are outside of the scope of this work.

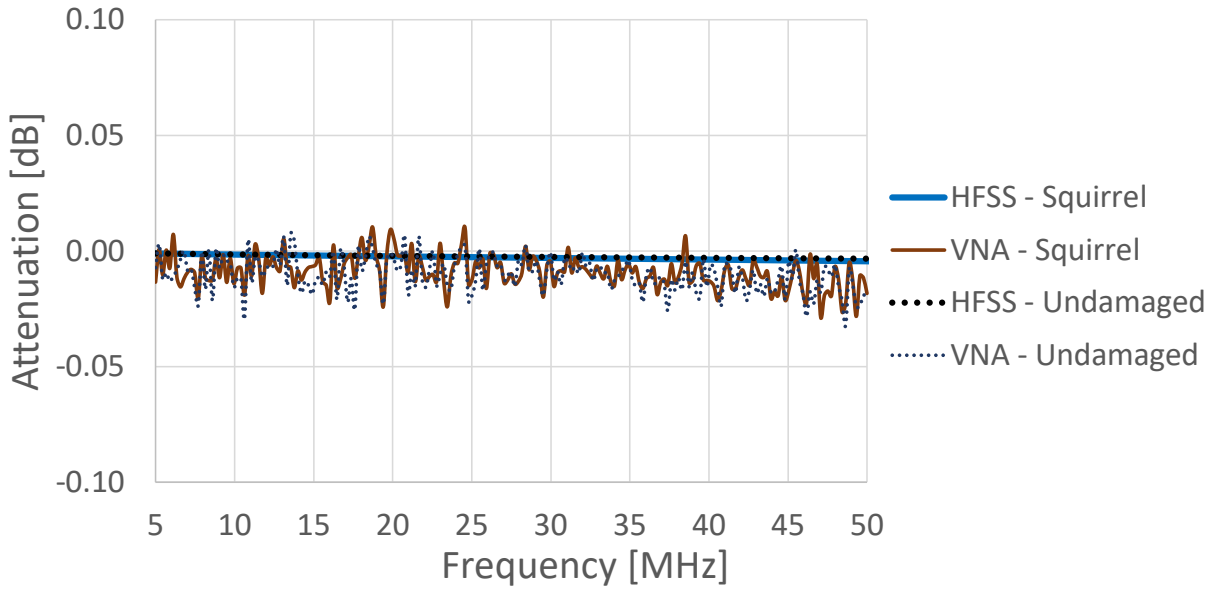

Fig. 32. Power budget of Pseudo squirrel-damaged vs. undamaged cable

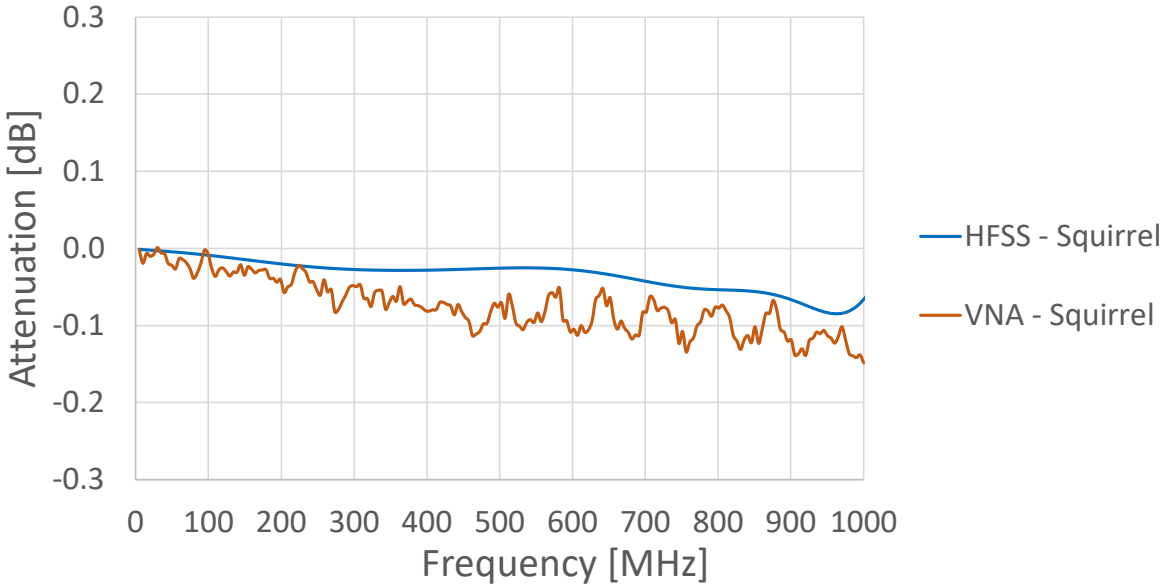

Fig. 33. Broadband power budget of squirrel-damaged cable

Given the premise that common-mode currents on the cable sheath exterior surface are a chief determinant of ingress or egress in the 5-50 MHz range, it would be expected that an absence of attenuation in the power budget (Fig. 32) would be accompanied by a lack of common-mode currents. To explore this, the HFSS simulation of the squirrel-damaged cable was used to plot the magnitude of the H field on a lateral section (Fig. 35) and at two cross-sections: one at the midpoint of the fault (25 cm), and also at a position on the cable closer to the source port where there was no damage to the sheath 5 (cm), as shown in Fig. 34. From these it can be seen that within the damaged section of cable, the H field does extend modestly beyond the bounds of the cable (Fig. 36a), however, in sections of the cable where the sheath is intact, no significant net H field is present outside the sheath conductor (Fig. 36b), indicating an absence of common-mode currents, as predicted. In work by Hayashi *et al*, it was found

that common-mode currents are sensitive and proportional to cross-fault resistance, and that at DC resistances approaching 0 Ω, common-mode currents are highly suppressed [19]. The remaining sheath in the compromised section presents an elevated resistance, as compared with an intact section, but the resistance is still extremely low (on the order of 200 $\mu\Omega$ at DC), and this suggests itself as an explanation for the observed lack of radiative losses.

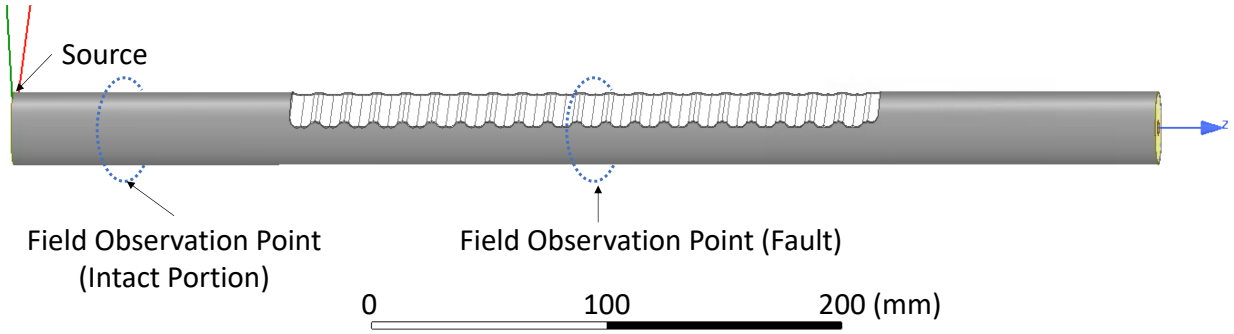

Fig. 34. Field observation points for modeled test cables

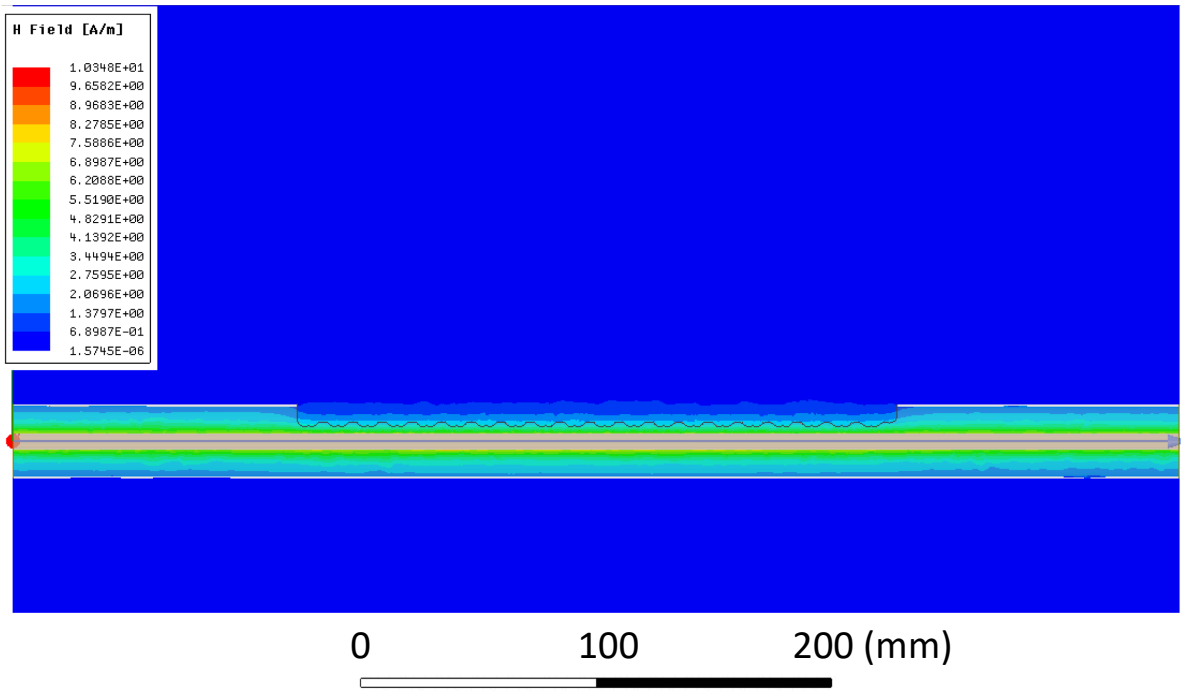

Fig. 35. Simulation of H field lateral sections of squirrel-damaged cable

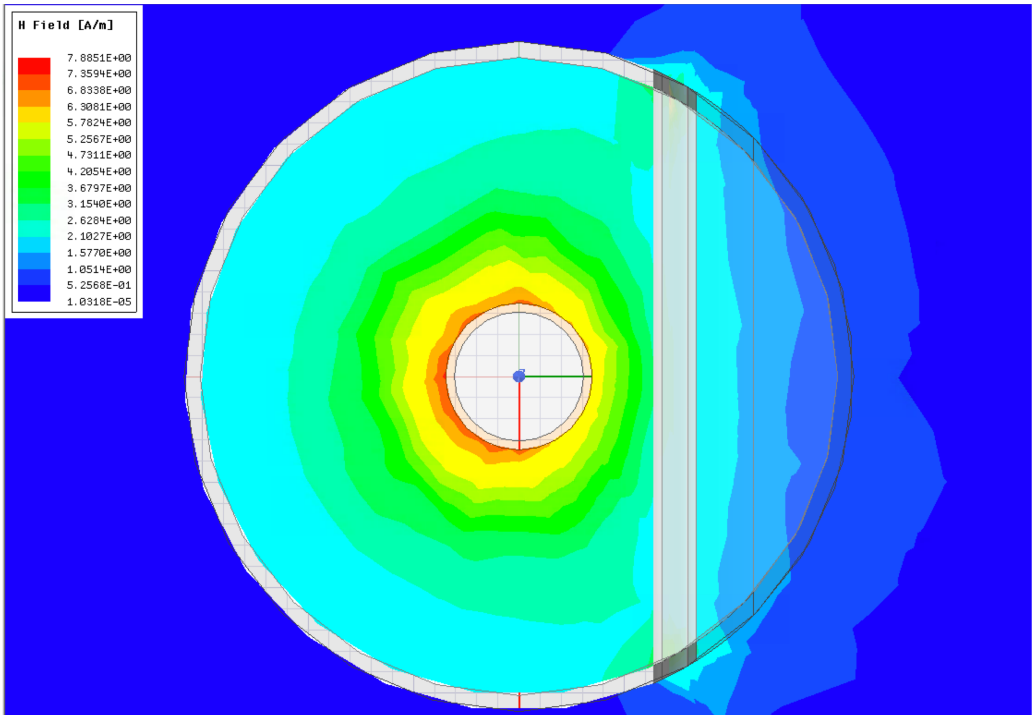

a) Cross section at midpoint of fault (25 cm)

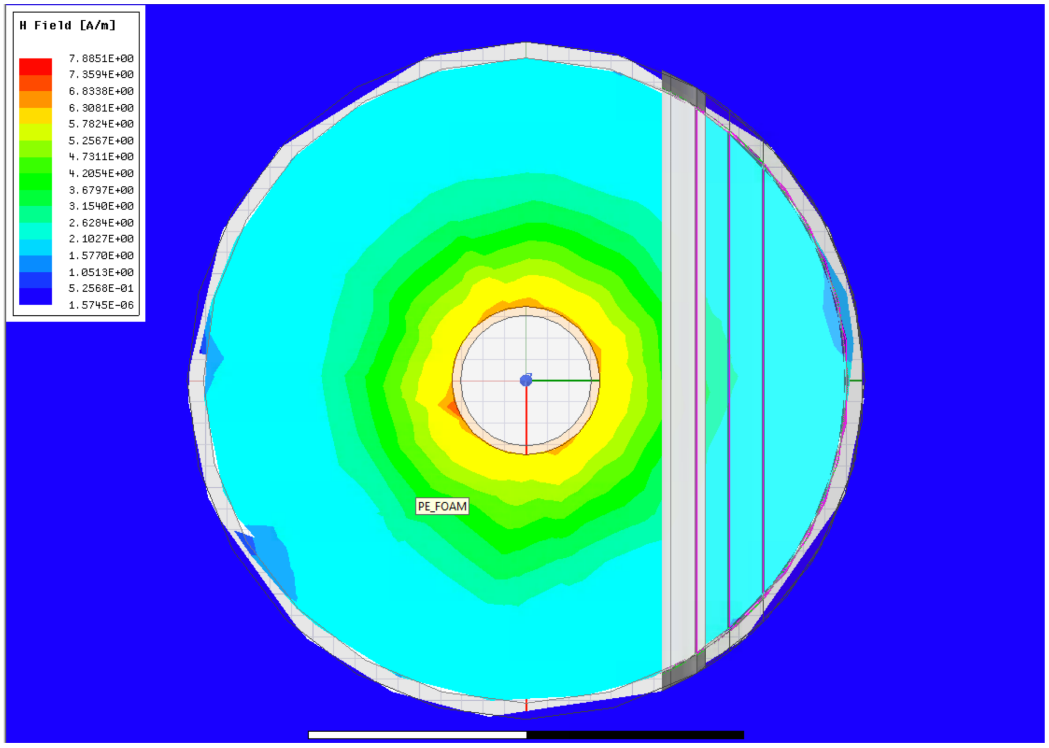

b) Cross section at source side upstream from fault (5 cm)

Fig. 36. Simulations of H field cross-sections of squirrel-damaged cable

5.3 Radial Cracked Cable

Unlike the pseudo squirrel-damage samples, it was found that across several different samples generated, the radial crack damage reliably produced the spectrum of interest (Fig. 37). On the ambient ingress test, a single radial crack fault was shown to produce ingress at levels on the order of 1 mV in the worst cases, which highlights the severity of the impact these faults can have on the operation of HFC networks in this band. This fact has been well documented by industry groups such as the SCTE [8]. These results are consistent with the findings of Nakamura *et al*, in their Fig. 6 [4], which depicts the typical ingress spectrum of a CATV return path (here reproduced in the left of Fig. 38), and of this author's prior field studies. Visual inspection of Fig. 37 and Fig. 38 reveal the similarities in their amplitude spectra.

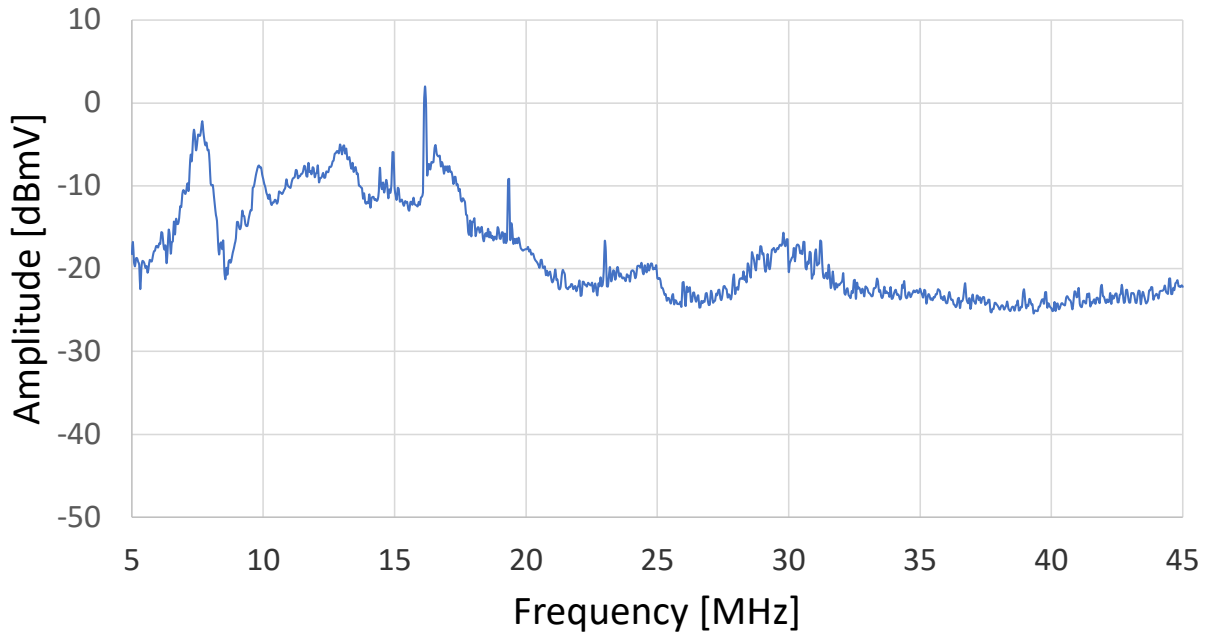

Fig. 37. Ingress spectrum of radial cracked cable

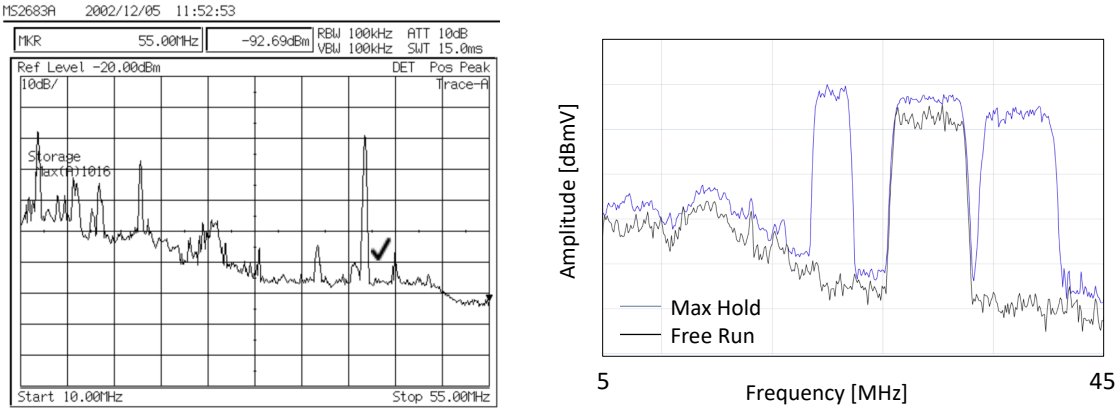

Fig. 38. CATV return spectrum showing ingress (left: reproduced from Fig. 6 of [4], right: from this author's field work)

Whereas in the power budget analysis (Fig. 39) the undamaged and squirrel-damages segments demonstrated near-perfect conservation of the injected signal (either by reflection or transmission) within the bandwidth of interest, the radial cracked cable substantially deviates from this 0dB line. Intriguingly, it showed both negative and positive variation, suggesting that power is being both lost to radiation and gained from ambient ingress, the latter then being added to the VNA's measurements for S_{11} and/or S_{21}. The presence of ingress power in the VNA measurements is perhaps unsurprising, given the results of the ambient ingress test discussed above and transmission/reception reciprocity.

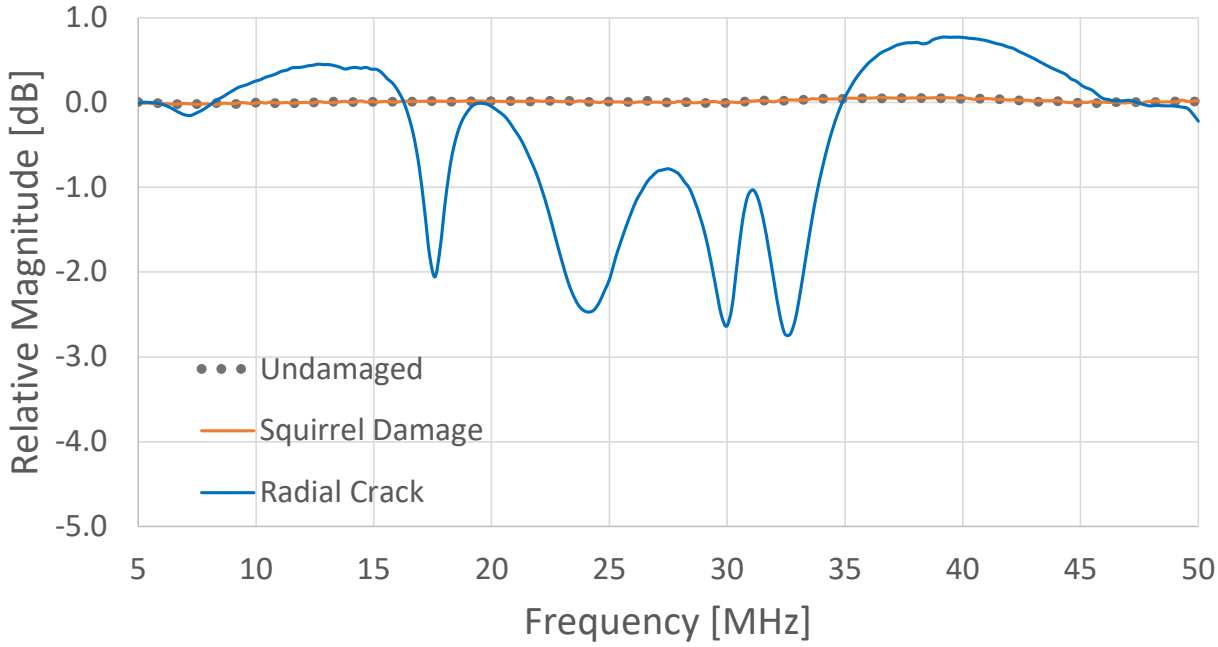

Fig. 39. Power budget of test cables from VNA readings

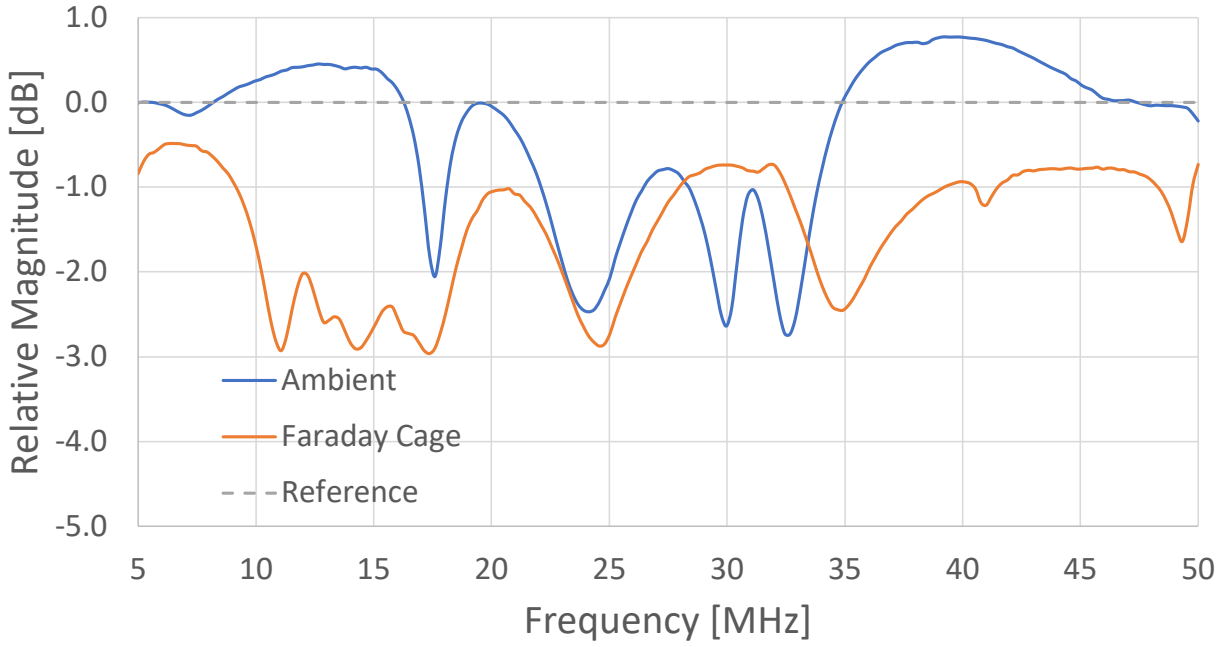

Fig. 40. Anechoic chamber vs. ambient power budget of radial cracked cable

To corroborate this interpretation, VNA tests were repeated while the entire setup (VNA, cable under test, etc.) was installed in an anechoic chamber. It was found that when isolated from ambient ingress, the power budgets of the radial cracked segments indeed showed only radiative losses. A comparison of two such cases is shown in Fig. 40. In light of this, unless otherwise stated, VNA data presented will be for tests conducted inside the anechoic chamber.

5.3.1 Modeled vs. Observed S-Parameters

Despite the geometric idealizations made in the HFSS model for the radial crack as compared with the complexities of the physical exemplar, the two sets of data showed reasonable agreement (Fig. 41 and Fig. 42). The VNA measurements were more feature rich, as compared with the results from the HFSS model, but the broad trend of relative magnitude vs. frequency tracked well, with the former resembling trend lines for the latter. It was not determined what properties governed the sharper peaks and valleys with respect to frequency in the VNA measurements, such as the valley that can be seen at approximately 38 MHz for test samples 03 and 04 in Fig. 42, but they were found to be unstable, varying in magnitude and precise frequency with time, handling of test segments, and across individual measurements for a given test segment. As discussed briefly in subsequent sections, there are some indications that factors such as cable length may influence these features, but their precise nature is beyond the scope of this work.

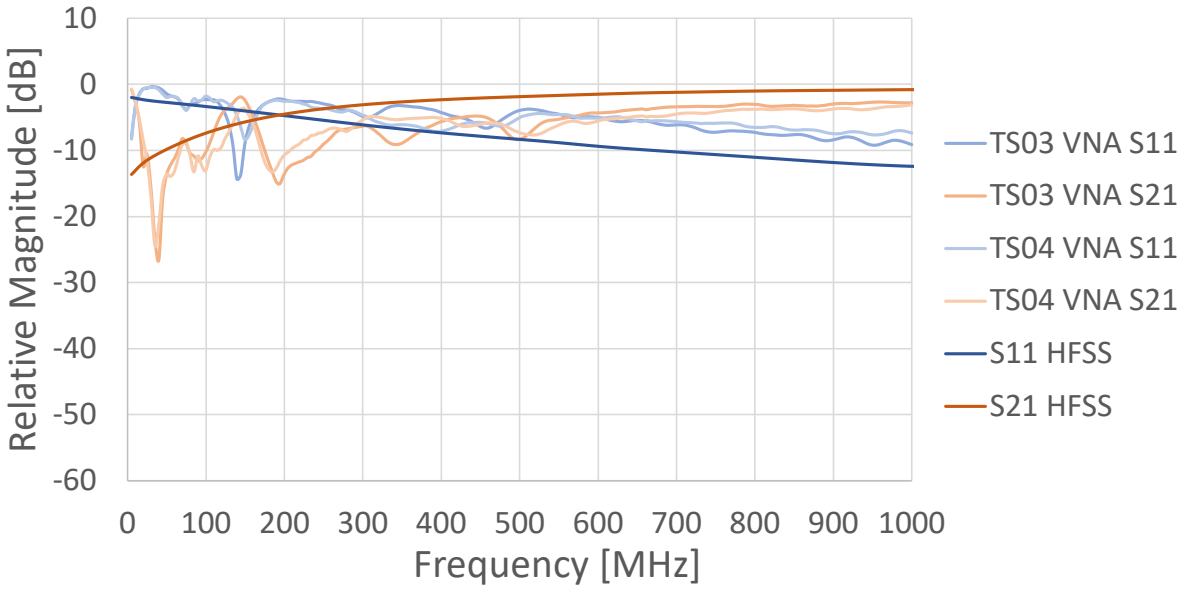

Fig. 41. Modeled and empirical S-parameters of radial cracked cable, 5-1000MHz

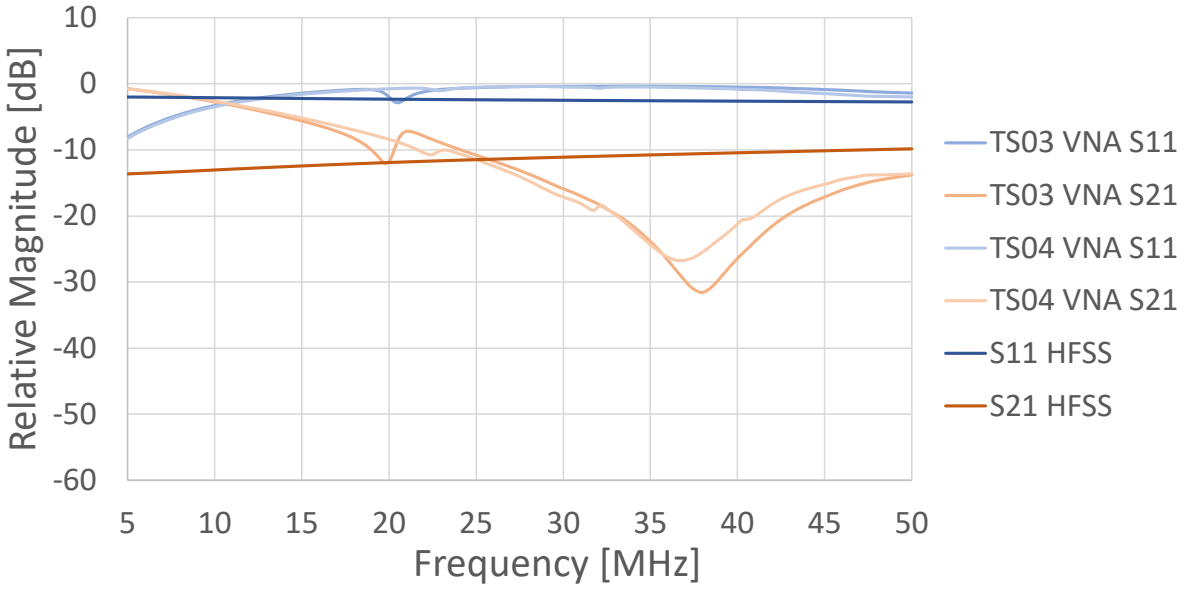

Fig. 42. Modeled and empirical S-parameters of radial cracked cable, 5-50MHz

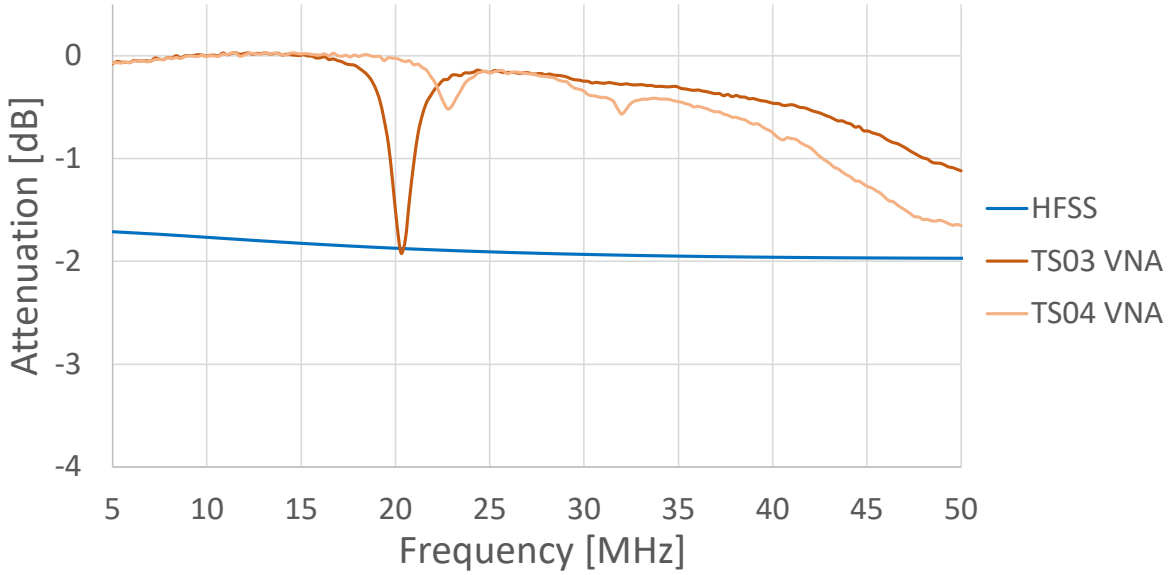

Fig. 43. Power budget of modeled and actual radial cracked cables

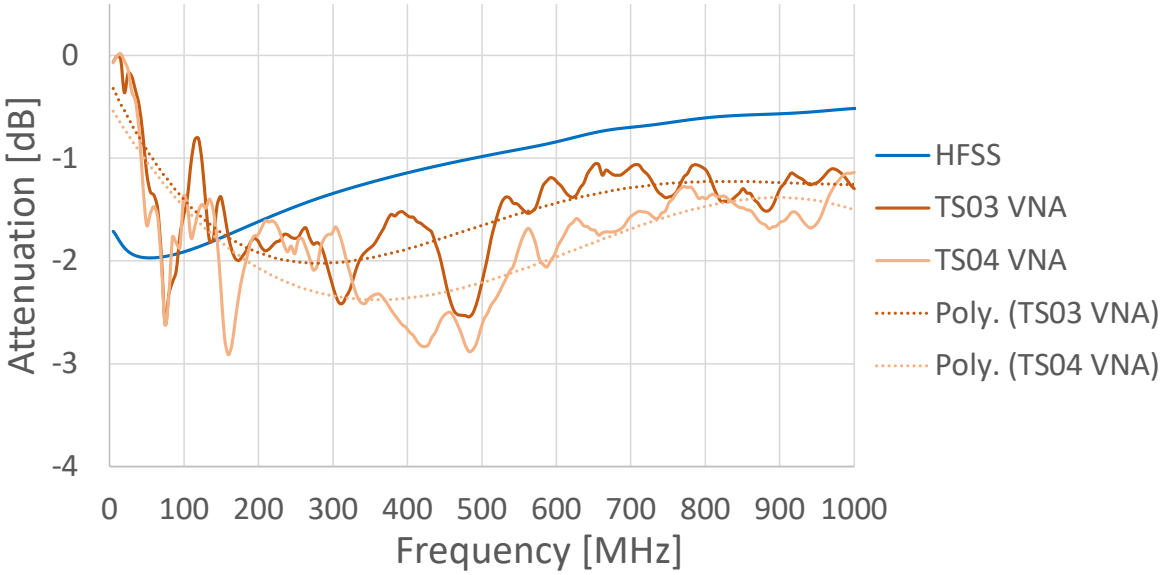

Fig. 44. Broadband power budget of modeled and actual radial cracked cables

While the HFSS models did not reproduce every detail of the empirical observations, they were found to broadly agree with the radiative properties of the test

cables they were meant to represent, as can be seen in Fig. 43 and Fig. 44, where the modeled attenuation due to radiative losses was of the same order of magnitude as the empirical observations, and followed the same overall pattern of variation with frequency. This is coupled with agreement between the model and empirical results for the undamaged and pseudo squirrel-damaged cables where both had a lack of radiative losses, which lends confidence in the suitability of the HFSS simulations as proxies for the physical specimens.

5.3.2 Peripheral Factors: Fault Position and Overall Cable Length

The role played by fault position on the radiative properties of test cables was explored in several ways. Firstly, the power budget of a radial cracked segment whose fault was offset from the center of the cable (test cable 04 from Table 1) was measured in two configurations: once with the source lead of the VNA nearer the fault, and once with the source and receive leads connected in the opposite way, so that the source lead was farthest from the fault. The results of this experiment can be seen in Fig. 45. While the near-fed and far-fed variants are not identical, they are very similar, and the differences are within the range of inter-trial variation observed for these tests, due to subtle rearrangement of the gap geometry, cable routing, etc. This is perhaps more clearly seen in Fig. 46, where several test segments (02, 03, and 04), were connected to a 12m section of undamaged cable and a similar test as before conducted, where a power budget was calculated for each in both near-fed and far-fed configurations. Again, the frequency response is not identical from near-fed to far-fed for a given cable, but the overall frequency response is largely stable in the broad trends.

On the other hand, increasing the overall length of the cable did have a consistent and noteworthy impact on the radiative properties. The difference can be seen in Fig. 47, where the power budgets of the three radial crack test cable were measured while they were connected directly to the VNA and also while they were connected to the undamaged 12m section of cable, making an overall longer cable assembly. There is more power missing overall from the VNA measurements, indication greater radiative losses, and those losses form more pronounced valleys in the plot. As noted previously, the precise magnitude and frequency of these features in the response are not stable and are subject to variation in conjunction with a set of only partially identified parameters. What is important for this work is that the cables with radial cracks consistently demonstrate radiative losses of comparable magnitude for a given cable length, and that these properties are replicated in the HFSS models.

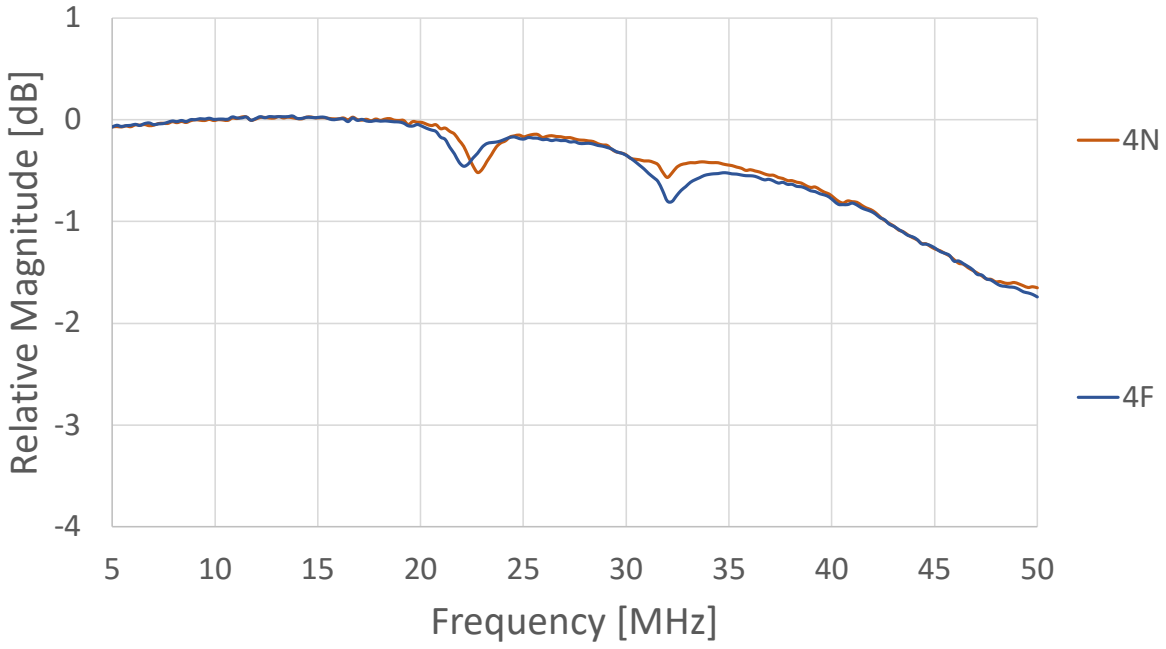

Fig. 45. Power budgets of test cable 04 fed from end nearer or farther from fault

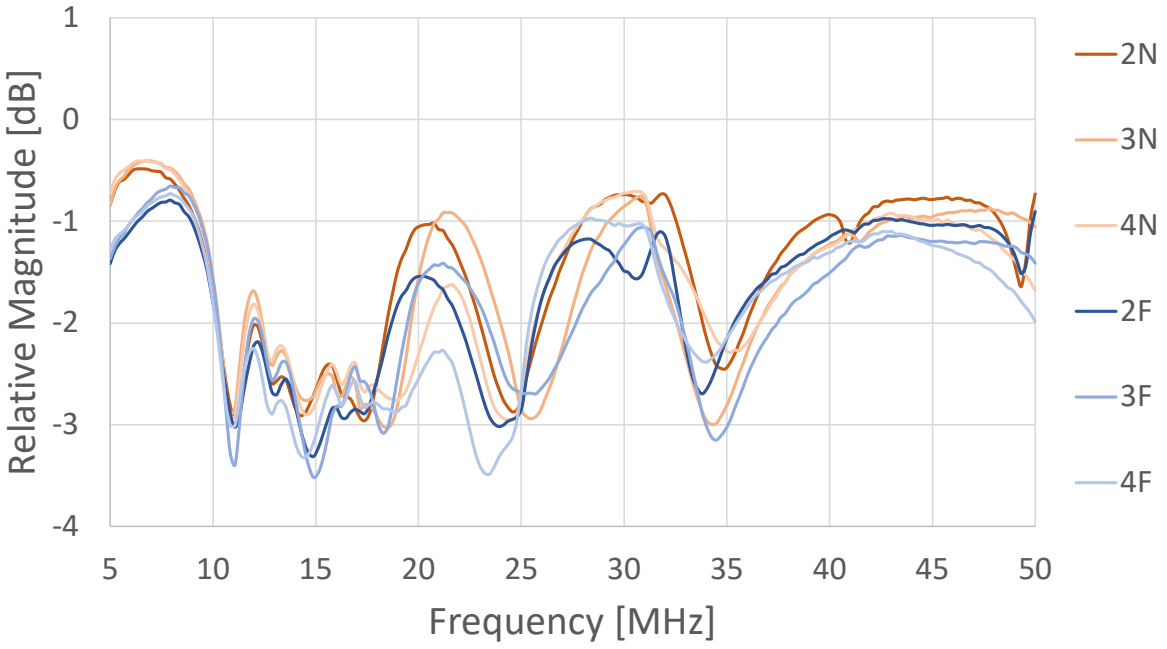

Fig. 46. Near vs. far power budgets of test cables 02-04 attached to 12m cable section

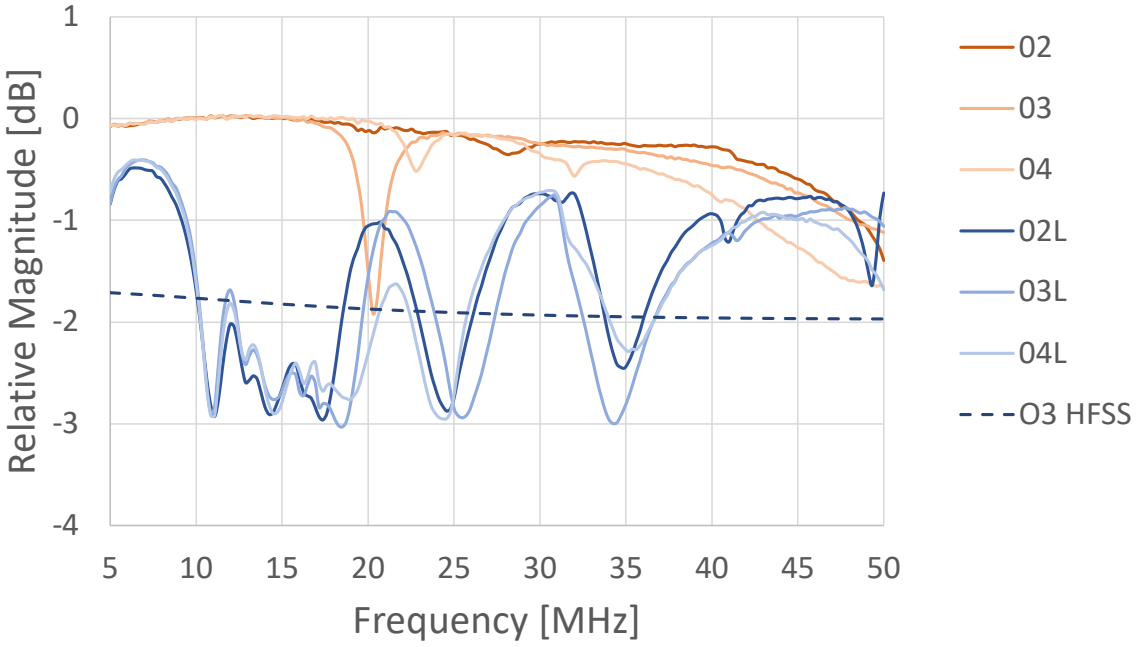

Fig. 47. Power budgets of test cables 02-04 independently vs. connected to 12m cable section

5.3.3 Common-mode Currents as a Causal Mechanism

If the hypothesis holds that the observed radiative properties of the test cables examined by this work are the result of the common-mode currents that develop in response to sheath faults, then several testable conditions present themselves. Firstly, if there were some way to attenuate the common-mode currents, then some reduction in the attenuation due to radiative losses would be expected. A schematic representation of a transmission line with common-mode currents traveling on the outer surface of the sheath conductor is shown in Fig. 48. A suppression of the common-mode currents would be equivalent to a substantial increase in R_{CM} in this representation. Another prediction would be that if a sufficiently low resistance short across the radial crack fault (C_{Gap} below) were introduced, then according to findings by Hayashi *et al*, a significant reduction in common-mode currents, and therefore radiative losses, should be observed [18, 19]. Lastly, if common-mode currents are suspected as the causal mechanism for radiative losses (and through reciprocity for ingress intrusion), and given HFSS simulations of radial cracks that reproduce such losses, we would expect to find evidence of common-mode currents on the outside of the sheath conductor in those simulations. Fortunately, all three of these predictions can be tested, and are discussed below.

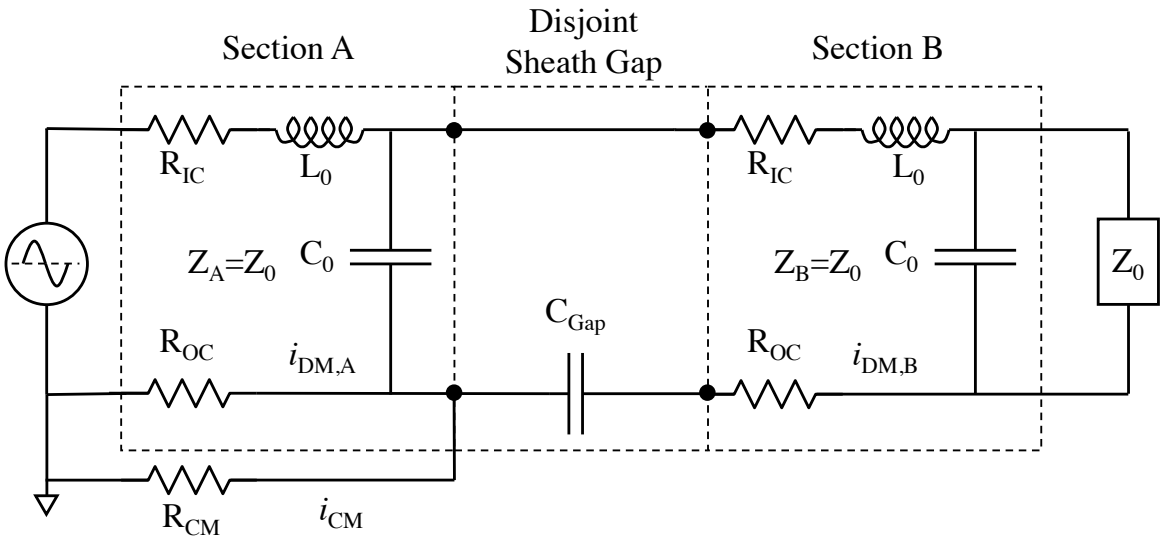

Fig. 48. Lumped element model of a common-mode current path on a coaxial transmission line

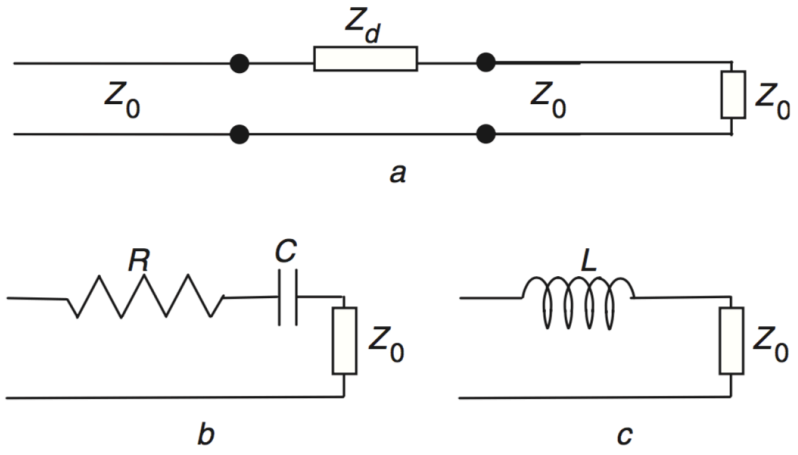

Fig. 6 *Equivalent circuit and impedances*
a Equivalent circuit for the series discontinuities considered in the paper
b Equivalent impedance of the annular interruption closed on the cable impedance
c Equivalent impedance of the small hole in the shield closed on the cable impedance

Fig. 49. Reproduction of Fig. 6 from Cerri *et al* [13]

Before moving on to the results of these tests, it should be noted that while lumped element models such as Fig. 48 are illustrative for visualizing features such as the path that common-mode current takes, and the point at which common-mode to differential-mode conversion would occur, it is not directly suitable for use as a simulation of the phenomenon. Work by Cerri *et al* has shown that sheath faults are better represented in lumped element models as a combination of series resistances, inductances, and capacitances in the signal line [13], which would be the center conductor of Fig. 48. A reproduction of a figure from Cerri *et al* shows how small sheath holes or disjoint gaps, or an "annular interruption", in their words, might be represented on a coaxial transmission line model. Such models, however, do not directly simulate common-mode currents and merely use the series resistance of part b in Fig. 49 as a radiation-resistance, which serves to include the effect of radiative losses without representing their underlying mechanism. Brown and Whitlock demonstrated a similar inclusion of radiative losses due to common-mode currents in lumped element models utilizing coupled inductors [25]. Since these approaches assume the phenomenon this work is trying to demonstrate, they are not useful to the immediate purpose.

To validate the first of the above predictions, power budgets derived from VNA S-parameter readings were processed for two of the test segments with radial cracks both with and without the addition of ferrite beads around the cable in question. The results of this exercise are shown in Fig. 50, where the numbers in the legend indicate the test segment number from Table 1, and the "Fe" suffix indicates the presence of ferrite beads for that trial. If common-mode currents were present and responsible for radiative losses,

then these ferrite beads should act as chokes and increase the effective impedance for them. While a substantially complete rejection of common-mode currents would likely require more than the 10 beads used in this case (or somehow to get multiple loops of wire through an individual ferrite bead), the addition of ferrites around the cable appears to have had the expected damping effect.

As can be seen in Fig. 52, not only do substantial H field magnitudes exist in the immediate vicinity of the simulated fault (Fig. 52a), but these extend from the outer surface of the sheath conductor even at some distance away from the fault itself (Fig. 52b). This can also be seen in the lateral cut view (Fig. 51) extending the length of the simulated cable segment. These H fields suggest the presence of common-mode currents, and these results should be compared with similar plots generated for the undamaged (Fig. 29) and pseudo squirrel-damaged cables (Fig. 36), where there was no appreciable H field on the outer sheath in the HFSS simulation, and also no appreciable radiative loss in the band of interest.

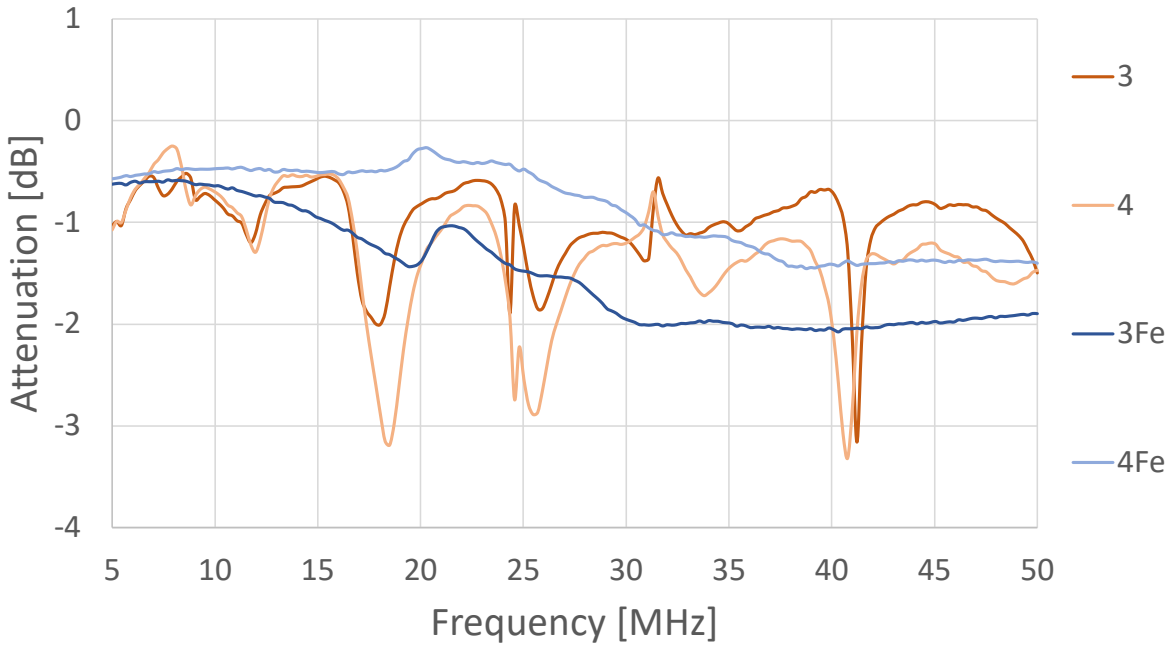

Fig. 50. Choked vs. unchoked test cable power budget

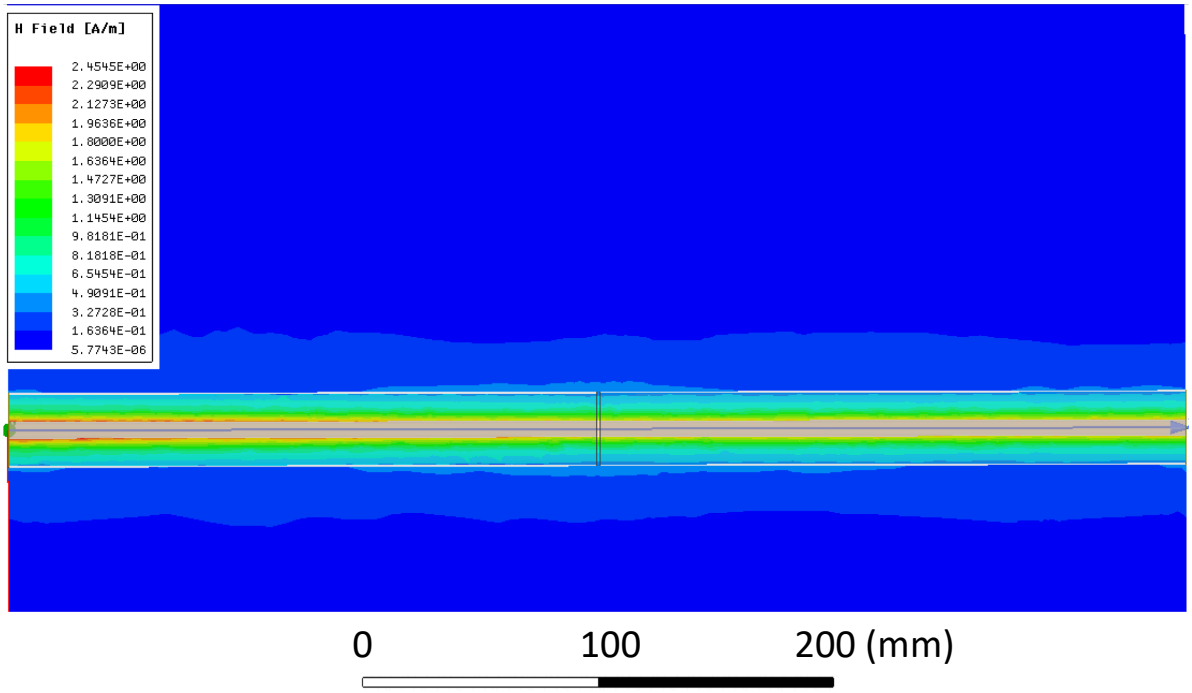

Fig. 51. Simulation of H field lateral section of radial cracked cable

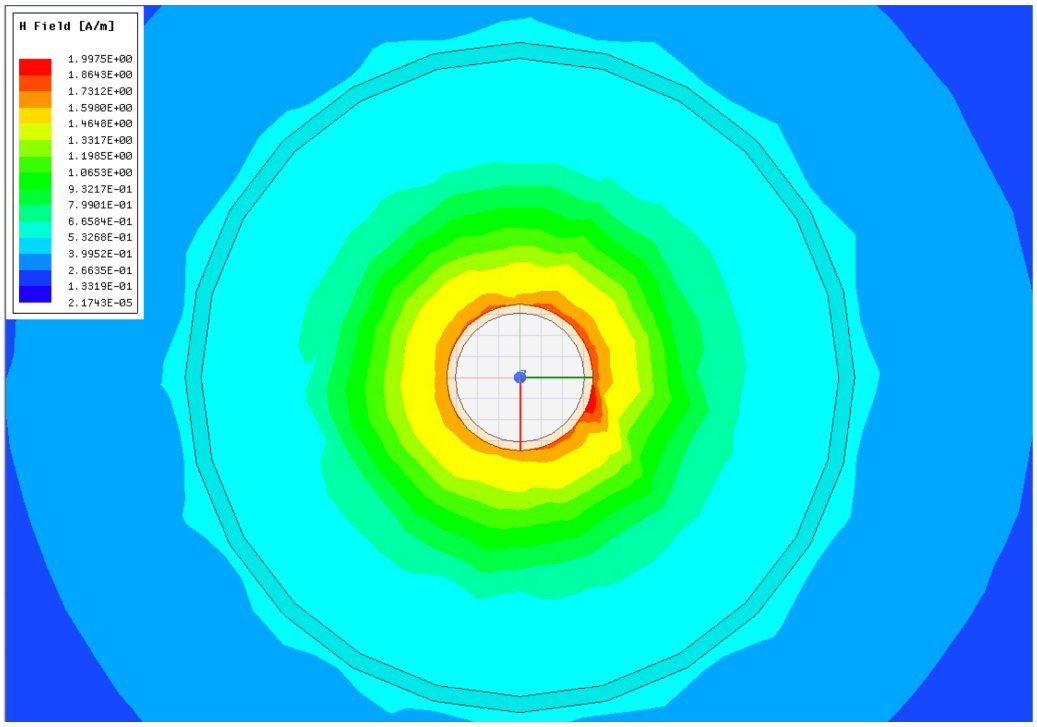

a) Cross section at point of fault (25 cm)

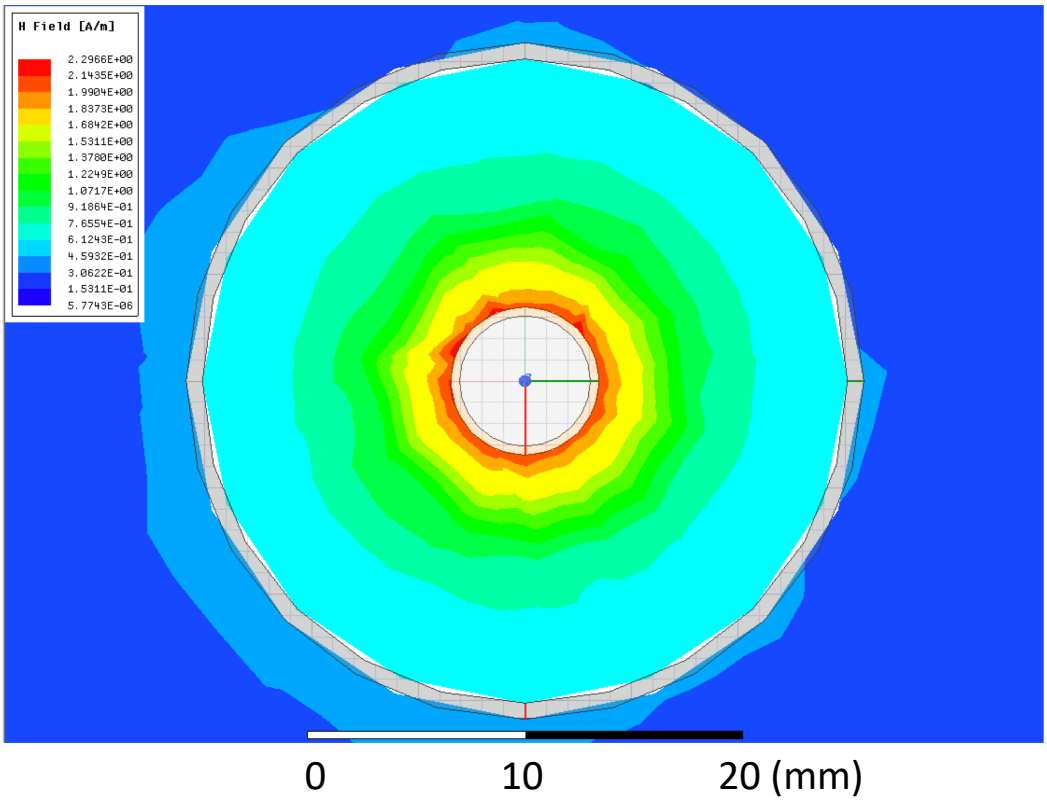

b) Cross section at source side upstream from fault (10 cm)

Fig. 52. Simulations of H field cross-sections of radial cracked cable

5.3.4 Effects of Resistive Bridges

Another permutation on the radial crack fault case exists when the fault is not disjoint, either because the two side of the sheath produced by the radial crack maintain some amount of contact, or a physically disjoint radial crack is bridged by some electrical path, such as a resistor or conductor. This corresponds to R_{Gap} in Fig. 53. As mentioned previously, work by Hayahsi *et al* would predict that a radial gap bridged by a resistance element (on the order of as little as 1 Ω at DC) will produce common-mode currents, and that within a certain range these currents will increase as overall gap resistance increases [18, 19]. Conversely, a conductive bridge across the gap of the radial crack approaching 0 Ω at DC should significantly favor differential-mode currents over common-mode and thereby reduce radiative losses. As can be seen in Fig. 54, the effect of shorting a single point across a radial crack gap with a good conductor has the effect of almost entirely eliminating its radiative losses and is therefore consistent with expectations.

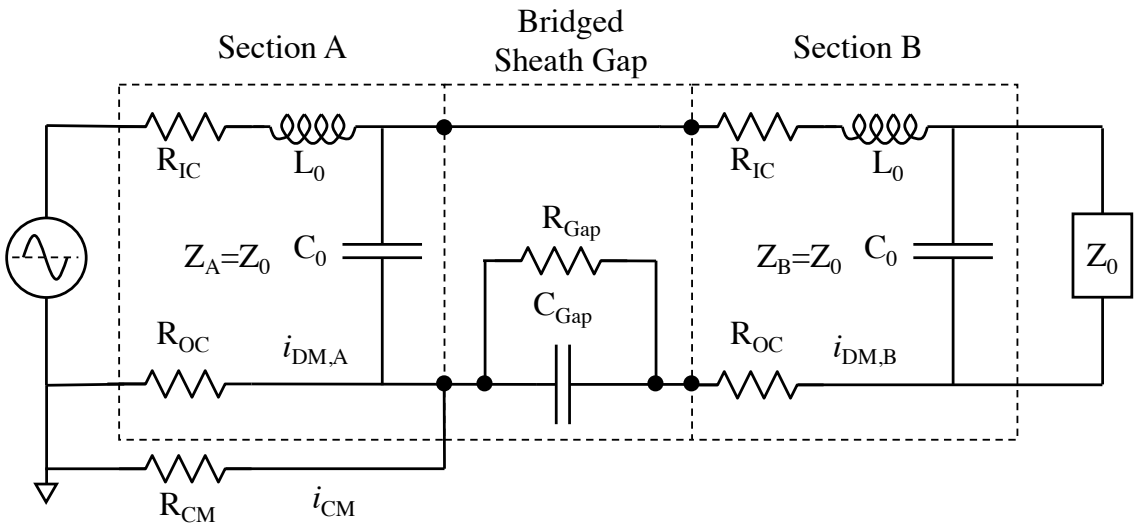

Fig. 53. Lumped element model of a bridged sheath gap fault

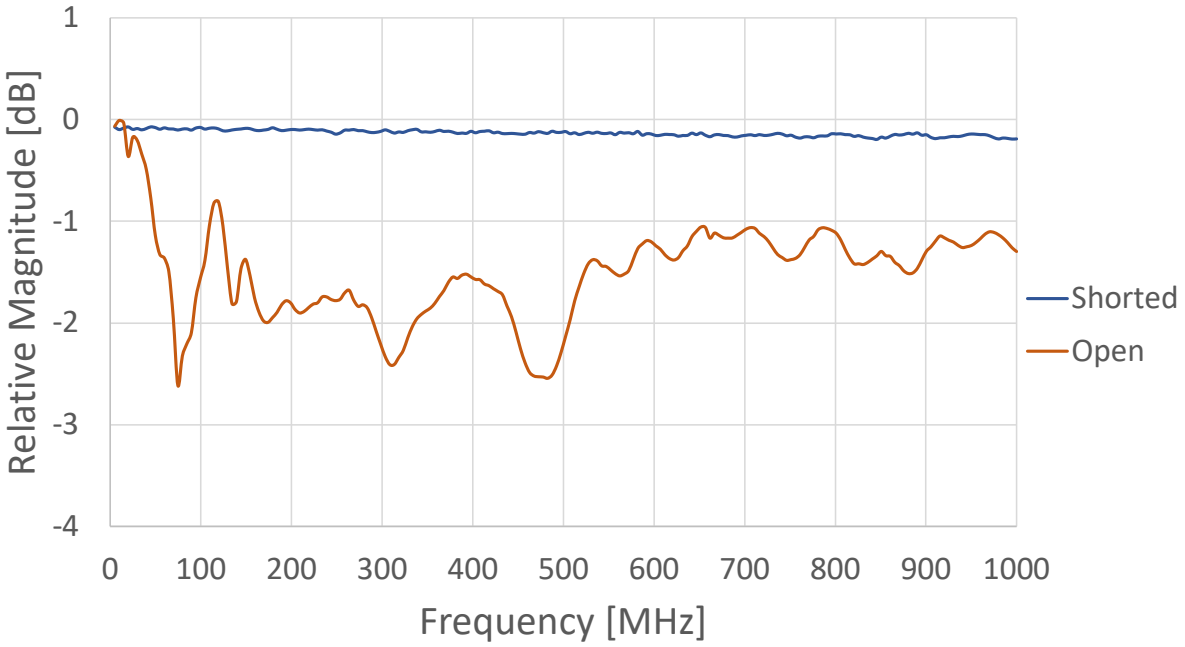

Fig. 54. Power budget of a radial cracked cable with and without a bridge short

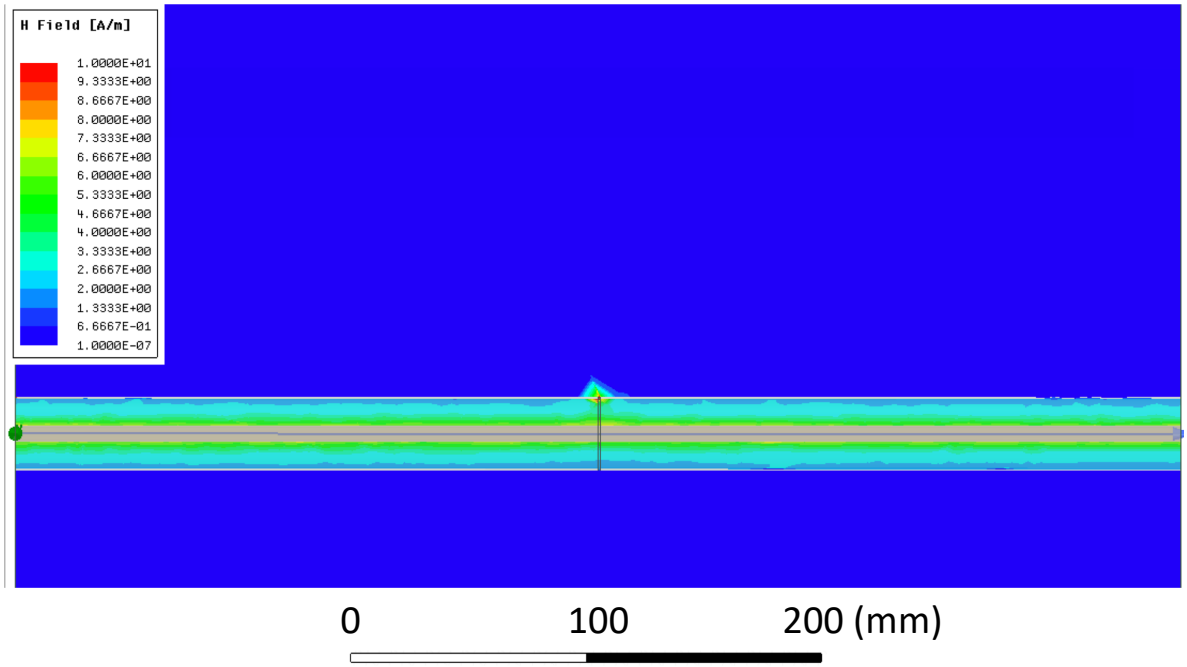

Figure 55. Simulation of H field lateral section of a shorted radial crack

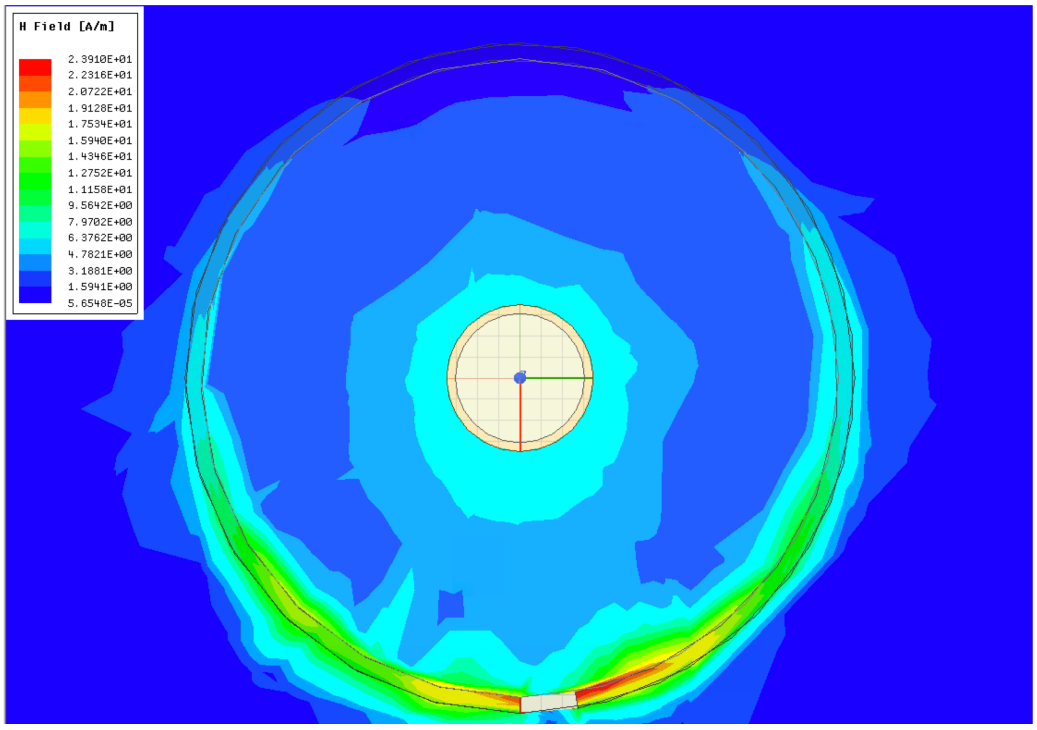

a) Cross section at midpoint of fault (25 cm)

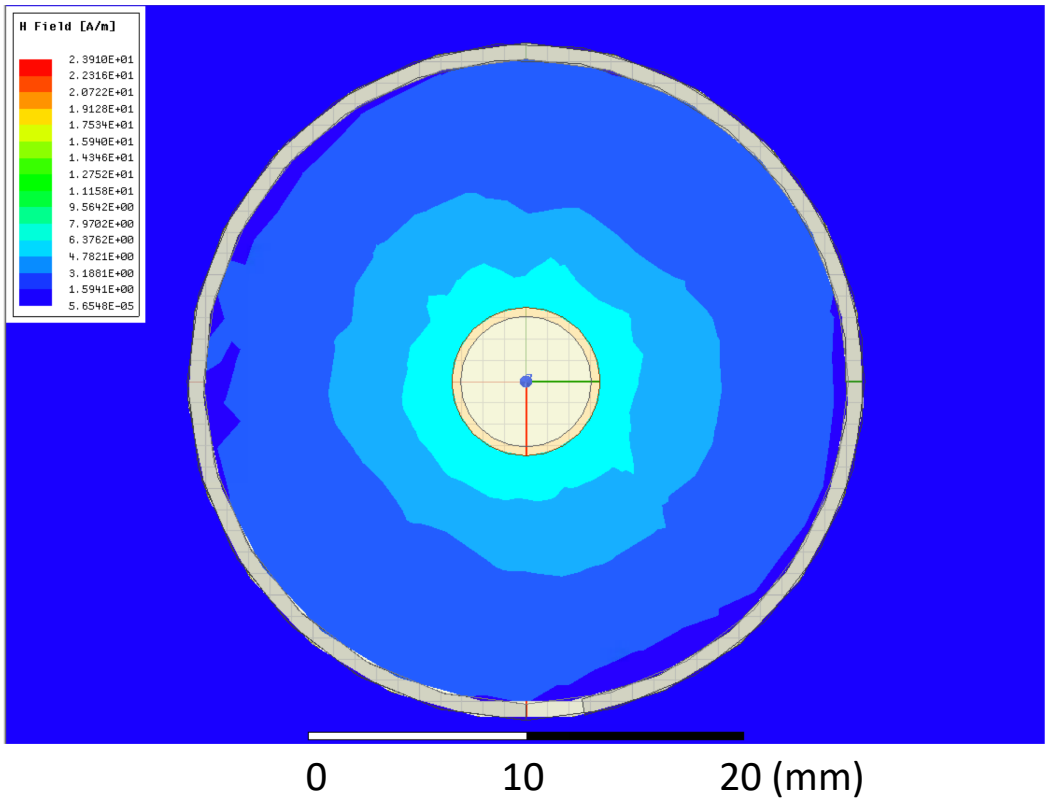

b) Cross section at source side upstream from fault (5 cm)

Fig. 56. Simulations of H field cross-sections of a shorted radial crack

The HFSS simulation was found to be consistent with the empirical observations. In Fig. 56, non-zero H field magnitude can be seen in the vicinity of the fault (Fig. 56a), but it is significantly more contained than for the unbridged gap, and there is no indication of H fields outside of the sheath conductor at a distance from the fault (Fig. 56b). Again, this is consistent with expectations and further supports the hypothesis that common-mode currents arising from sheath faults are indeed the causal mechanism for the observed ingress and egress phenomena. Fig. 57 shows the close agreement between the simulated and empirical results of shorting across a disjoint radial crack.

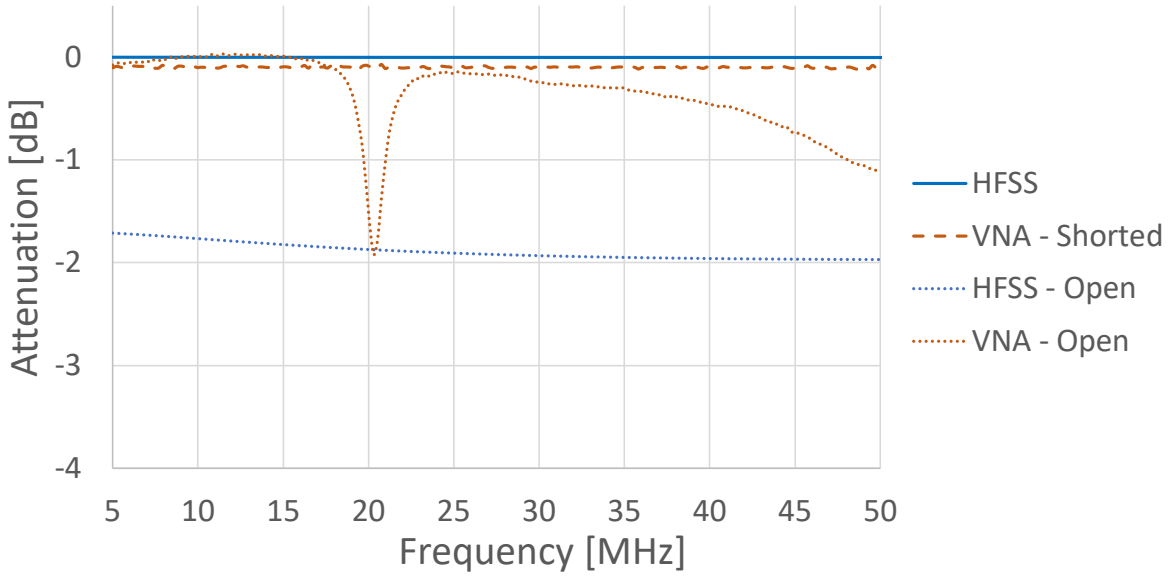

Fig. 57. Comparison of empirical and modeled effects of shorted radial crack gap

Another variation on this test was performed with a test cable (segment 02 from Table 1), in which the two sides of the radial crack made partial contact. This specimen was manipulated until it exhibited a positive response on the ingress spectrum test and then splinted to maintain its physical orientation as much as possible. The DC resistance

across the gap so constructed was highly sensitive to variation, but nevertheless stayed generally in the 0.5 Ω to 1.5 Ω range. An HFSS simulation of this test cable was made by producing a conductive bridge similar to that depicted in the bottom part of Fig. 56a, but much narrower, in an attempt to increase its resistance. The results of both the empirical measurements and the simulation are shown in Fig. 58. The VNA measurements produced clear signs of radiative losses. However, it is worth noting that the magnitude of these losses are somewhat less than the fully disjoint radial gaps of test segments 03 and 04 (Fig. 43). This is again consistent with the findings of Hayashi *et al*, where a moderate fault gap resistance would produce intermediate levels of common-mode current and therefore radiative losses [19]. It was also found that if the cable segment was manipulated such that the two sides of the sheath made solid contact, i.e., 0 Ω measured across the gap at DC, the radiative losses disappeared.

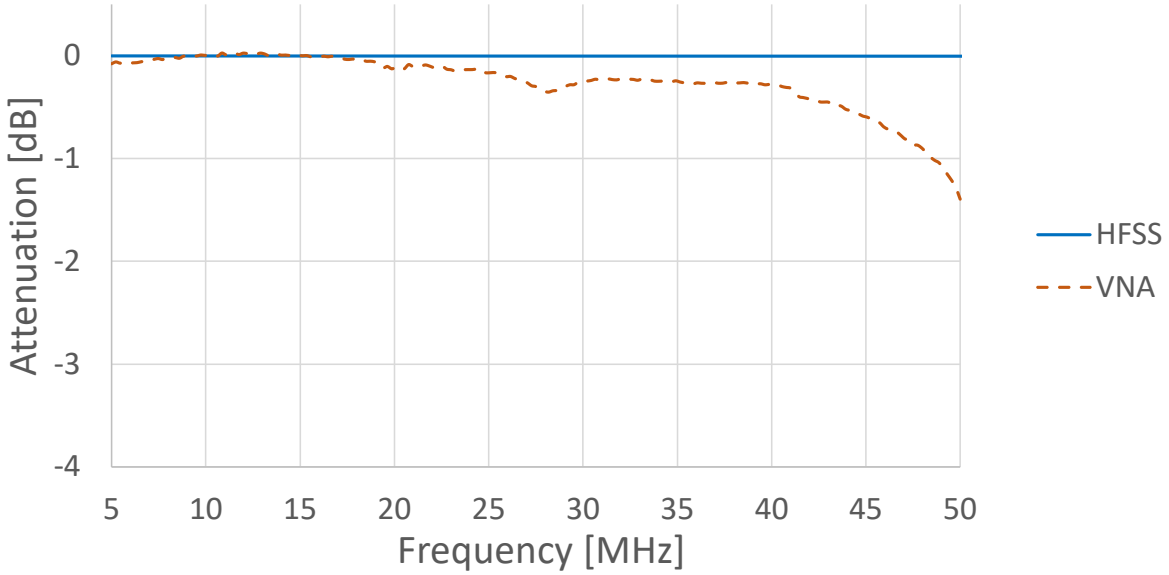

Fig. 58. Simulated and observed power budget for resistively-bridge radial crack

Unfortunately, the simulation of the resistive bridge mechanism was not successful. It was found that the bridging element was either too large in cross-sectional area to yield sufficiently small resistance values in the model, or that model would start to behave unpredictably if, in an effort to achieve higher resistance, its size was reduced below a certain threshold. Alternate mechanisms to model this permutation will be left to future work.

5.5 Conclusion

While the simulations did not reproduce every aspect of the physical observations, there was reasonable agreement in several key respects, which lends validity to the overall experimental design. Results obtained were consistent with a number of aspects of prior work, which also gives confidence in the findings of the current work. Various predictions of the hypothesis of common-mode currents as a signal leakage mechanism were tested for their agreement with expectations, and these predictions were confirmed by the experimental findings.

The results of the various test cases are summarized in Table 3. It can be seen that there is a strong correlation between the presence of common-mode currents in the HFSS model and ingress or egress from the cables as empirically observed via the ambient ingress spectrum or S-parameter power loss tests. This supports the hypothesis that the common-mode to differential-mode conversion (or vice-versa) is the primary mechanism underlying the observed ingress or egress phenomena. Another suggestion of these findings is that differential behavior of certain fault conditions over others can be

explained by whether or not they provide for all of the conditions necessary for the formation of common-mode currents (Table 4).

Table 3. Summary of test results

Test Cable Type	Ambient Ingress Reception	Radiative Losses (VNA)	Radiative Losses (HFSS)	Common-Mode Currents (HFSS)
Undamaged	No	No	No	No
Pseudo Squirrel-damaged	No	No	No	No
Disjoint Radial Crack	Yes	Yes	Yes	Yes
Shorted Radial Crack	No	No	No	No
Resistively Bridged Radial Crack	Yes	Yes	-	-

Table 4. Survey of test cable fault properties

Test Cable Type	Path to Sheath Exterior	Impedance Mismatch	Sufficient Cross-Fault Resistance
Undamaged	No	No	No
Pseudo Squirrel-damaged	Yes	Yes	No
Disjoint Radial Crack	Yes	Yes	Yes
Shorted Radial Crack	Yes	Yes	No
Resistively Bridged Radial Crack	Yes	Yes	Yes

5.4 Future Work

Future work would include a number of refinements to the models themselves, with the expectation that they could be made to even more closely mirror their physical counterparts. For example, in some of the test cable segments, the two surfaces of the radial crack have points of contact between one another, which produce resistive bridges that have so far eluded efforts herein to accurately simulate in HFSS.

Another point of interest that was observed but not explored by this work are the peaks in power loss at various frequencies that were present in the VNA readings, but not in simulation. It has been noted that sheath faults can exhibit frequency selectivity [8], and this may be one of the factors that contribute to it. The broader subject of frequency selectivity, and how the signal leakage mechanism explored in this work might relate to it, is a potential subject for future work.

Also, it has been noted in field studies that a variety of sheath holes (from squirrels and other sources) can be strong radiators in the band of interest [8], but the samples of this sort produced in the lab so far have failed to have similarly strong radiation. Further work to reproduce this effect is desired, since there may be mechanisms responsible for their strong radiative behavior that differ from the radial crack case. On this last point, it is speculated that the lack of ingress exhibited by some of the specimens could be due to a compromised sheath being necessary for common-mode currents to develop, and thereby ingress (or egress), but that compromised sheath is not by itself sufficient. It is possible that high-resistance on the sheath side of the circuit, for example, must also exist to give rise to the phenomenon. This is suggested by the results of the present work, and

by the findings of Hayashi *et al* [19, 20]. It has been noted that amongst the many faults found in surveys of HFC networks, that loose, weathered, or improperly installed cable connectors are a common finding [3, 8]. It is possible that that these provide the requisite resistance in conjunction with some other, more physically obvious fault. This hypothesis is left for future work to probe.

APPENDIX A – Calculations of Cable Characteristics (Mathematica)

Commscope P3 0.625 Characteristics

```
mpkf = 304.8;                          μ = 4 π * 10^-7;
cpm = 50.2 * 10^-12;
inOhmspfk = 0.84;                      outOhmspkf = 0.26;
sheathOuterR = 15.875 * 10^-3 / 2;     sheathThickness = 0.7620 * 10^-3;
centerCondD = 3.480 * 10^-3;
ϵ = cpm * Log[rout / rin] / (2 π);
ϵr = ϵ / (8.8541878 * 10^-12);
Lpm = μ / (2 π) Log[rout / rin];

Print["Center Conductor Resistance: ",
 (inOhmspm = inOhmspfk / mpkf) * 1000, " [mΩ/m]"]
Print["Sheath Conductor Resistance: ",
 (outOhmspm = outOhmspkf / mpkf) * 1000, " [mΩ/m]"]
Print["Sheath Inner Radius: ",
 (rout = sheathOuterR - sheathThickness) * 1000, " [mm]"]
Print["Center Conductor Radius: ", (rin = centerCondD / 2) * 1000, " [mm]"]
Print["Relative Permitivity, ϵr: ", ϵr]
Print["Nominal Capacitance: ", cpm * 10^12, " [pF/m]"]
Print["Nominal Inductance: ", (Lpm = μ / (2 π) Log[rout / rin]) * 10^9, " [nH/m]"]
Print["Characteristic Impedance (calculated): ", Sqrt[Lpm / cpm], " [Ω]"]
```

```
Center Conductor Resistance: 2.75591 [mΩ/m]
Sheath Conductor Resistance: 0.853018 [mΩ/m]
Sheath Inner Radius: 7.1755 [mm]
Center Conductor Radius: 1.74 [mm]
Relative Permitivity, ϵr: 1.27844
Nominal Capacitance: 50.2 [pF/m]
Nominal Inductance: 283.357 [nH/m]
Characteristic Impedance (calculated): 75.1304 [Ω]
```

Radial Crack Gap Capacitance Calculations

$$\text{gapFaceArea} = \int_{\text{rout}}^{\text{rout+sheathThickness}} 2\,\pi\,r\,dr;$$

```
Clear[d]
a = 0.1 * 10^-3; b = 1 * 10^-3; Δ = 0.1 * 10^-3; (*start, stop, and step of gap width*)
```

$$\text{Cgap}[d\_] := \frac{\epsilon\ \text{gapFaceArea}}{d};$$

```
Print["Approximate Gap Capacitance"];
Do[Print["d = ", d * 1000, " mm; C ≈ ", (Cgap [d]) * 10^12, " [pF]"], {d, a, b, Δ}]
```

```
Approximate Gap Capacitance
d = 0.1 mm; C ≈ 4.09528 [pF]
d = 0.2 mm; C ≈ 2.04764 [pF]
d = 0.3 mm; C ≈ 1.36509 [pF]
d = 0.4 mm; C ≈ 1.02382 [pF]
d = 0.5 mm; C ≈ 0.819057 [pF]
d = 0.6 mm; C ≈ 0.682547 [pF]
d = 0.7 mm; C ≈ 0.585041 [pF]
d = 0.8 mm; C ≈ 0.511911 [pF]
d = 0.9 mm; C ≈ 0.455032 [pF]
d = 1. mm; C ≈ 0.409528 [pF]
```

Misc. Factors

```
A = gapFaceArea;  ℓ = 1;  R = inOhmspm + outOhmspm;
```

$$\text{Print}\left["\rho\ =\ ", \rho = \frac{R\,A}{\ell}, "\ [\Omega\ m]"\right]$$

```
ρ = 1.30567 × 10^-7 [Ω m]
```

REFERENCES

[1] Code of Federal Regulations, Title 47, Part 76

[2] Hranac, R. and Murdock, T. UHF Leakage, Ingress, and Direct Pickup Impact on Spectral Efficiency. Proceedings of the SCTE Cable-Tec Expo, Society of Cable Telecommunications Engineers (2015). Retrieved October 11, 2017 from http://www.scte.org/Documents/KnowledgeCollection/Hranac_Murdock_Paper2015.pdf

[3] Steven Nielsen, Ronald Totten, Travis Halky. 2013. INGRESS-MITIGATED CABLE COMMUNICATION SYSTEMS AND METHODS HAVING INCREASED UPSTREAM CAPACITY FOR SUPPORTING VOICE AND/OR DATASERVICES, U.S. Patent 8,543,003, Filed September 24, 2013.

[4] M. Nakamura, Y. Yang, K. Wasaki and Y. Shidama, "Study on a noise reduction system of CATV network upstream for data communication," *Proceedings. 12th International Conference on Computer Communications and Networks (IEEE Cat. No.03EX712)*, 2003, pp. 613-616. doi: 10.1109/ICCCN.2003.1284235

[5] K. Haelvoet, J. Vandenbruaene, E. Claus, K. De Kesel and L. Martens, "Procedure for measurements and statistical processing of upstream channel noise in HFC-networks," *1998 IEEE MTT-S International Microwave Symposium Digest (Cat. No.98CH36192)*, Baltimore, MD, USA, 1998, pp. 1207-1210 vol.3. doi: 10.1109/MWSYM.1998.700591

[6] E. Sandino and C. Murphy, "HIGH-SPEED DATA SERVICES AND HFC NETWORK AVAILABILITY", in *NCTA Spring Technical Forum*, 1997.

[7] "Industry Data | NCTA", *Ncta.com*, 2018. [Online]. Available: https://www.ncta.com/industry-data. [Accessed: 30- Mar- 2018].

[8] Network Operations Subcommittee, "UHF Leakage, Ingress, Direct Pickup", Society of Cable Telecommunications Engineers, 2015.

[9] A. Manet, A. Kameni, F. Loete, J. Genoulaz, L. Pichon and O. Picon, "Equivalent Circuit Model of Soft Shield Defects in Coaxial Cables Using Numerical Modeling," in *IEEE Transactions on Electromagnetic Compatibility*, vol. 59, no. 2, pp. 533-536, April 2017. doi: 10.1109/TEMC.2016.2612719

[10] G. Cerri, R. De Leo, V. M. Primiani, S. Pennesi and P. Russo, "Electromagnetic characterization of faults on coaxial cable shields," *2004 International Symposium on Electromagnetic Compatibility (IEEE Cat. No.04CH37559)*, 2004, pp. 931-935 vol.3. doi: 10.1109/ISEMC.2004.1349950

[11] Effigis Geo Solutions, "USING THE GPS-BASED CPAT FLEX INGRESS DETECTION SOLUTION", 2018.

[12] Electromagnetic Simulation Products | ANSYS. Ansys.com, 2017. http://www.ansys.com

[13] G. Cerri, R. De Leo, L. Della Nebbia, S. Pennesi, V. M. Primiani and P. Russo, "Fault locatio o shielded cables: Electromagnetic modelling and improved measurement data processing," in *IEE Proceedings - Science, Measurement and Technology*, vol. 152, no. 5, pp. 217-226, 9 Sept. 2005. doi: 10.1049/ip-smt:20045035

[14] E. J. Lundquist, J. R. Nagel, S. Wu, B. Jones and C. Furse, "Advanced Forward Methods for Complex Wire Fault Modeling," in *IEEE Sensors Journal*, vol. 13, no. 4, pp. 1172-1179, April 2013. doi: 10.1109/JSEN.2012.2227996

[15] J. Brown, "Common impedance coupling of shield current at equipment inputs and outputs - the pin 1 problem - it's not only an audio problem!", *2005 International Symposium on Electromagnetic Compatibility*, 2005. EMC 2005.

[16] F. Han, "Radiated emission from shielded cables by pigtail effect," in *IEEE Transactions on Electromagnetic Compatibility*, vol. 34, no. 3, pp. 345-348, Aug 1992. doi: 10.1109/15.155852

[17] Mengxi Liu, Junjun Wang and Xuyue Wu, "Analysis of the radiation from a pigtail-terminated coaxial cable using the imbalance difference model," *2016 Progress in Electromagnetic Research Symposium (PIERS)*, Shanghai, 2016, pp. 2179-2183. doi: 10.1109/PIERS.2016.7734902

[18] Y. i. Hayashi, Y. Kayano, T. Mizuki, H. Sone and H. Inoue, "On contact conditions in connectors to cause Common Mode radiation," *2008 IEEE International Symposium on Electromagnetic Compatibility*, Detroit, MI, 2008, pp. 1-4. doi: 10.1109/ISEMC.2008.4652102

[19] Y. i. Hayashi, T. Mizuki and H. Sone, "Relationship between connector contact points and common-mode current on a coaxial transmission line," *2009 IEEE International Symposium on Electromagnetic Compatibility*, Austin, TX, 2009, pp. 209-212. doi: 10.1109/ISEMC.2009.5284621

[20] Y. i. Hayashi, K. Matsuda, T. Mizuki and H. Sone, "Investigation on the effect of parasitic inductance at connector contact boundary on electromagnetic radiation," *2012 Asia-Pacific Symposium on Electromagnetic Compatibility*, Singapore, 2012, pp. 65-68. doi: 10.1109/APEMC.2012.6237952

[21] Y. i. Hayashi, K. Matsuda, T. Mizuki and H. Sone, "Investigation on the effect of parasitic inductance at connector contact boundary on electromagnetic

radiation," *2012 Asia-Pacific Symposium on Electromagnetic Compatibility*, Singapore, 2012, pp. 65-68. doi: 10.1109/APEMC.2012.6237952

[22] P. Wang, M. C. Converse, J. G. Webster and D. M. Mahvi, ""Improved" Calculation of Reflection Coefficient for Coaxial Antennas With Feed Gap Effect," in *IEEE Transactions on Antennas and Propagation*, vol. 57, no. 2, pp. 559-563, Feb. 2009. doi: 10.1109/TAP.2008.2011411

[23] Keysight Technologies, "S-Parameter Design", 2014.

[24] Product Specifications for .625, 75 Ohm P3 Distribution Cable. Commscope, Inc., 2017.

[25] J. Brown and B. Whitlock, "Common-Mode to Differential-Mode Conversion in Shielded Twisted-Pair Cables (Shield-Current-Induced Noise)", in *114th AES Convention*, Amsterdam, 2003.